

Book of Abstracts

**THE 45TH ANNUAL SYMPOSIUM
ON POLYMER
SCIENCE/ENGINEERING**

**University of Waterloo
Waterloo, Ontario**

May 3th, 2023

**Institute for Polymer Research
University of Waterloo**

The Institute for Polymer Research would like to thank the sponsors for their support of the symposium.



2023

PROGRAM

**INSTITUTE FOR POLYMER RESEARCH
CELEBRATING 39 YEARS OF OFFICIAL INSTITUTE STATUS
FORTY-FIFTH ANNUAL SYMPOSIUM
ON POLYMER SCIENCE/ENGINEERING 2023
E7 7303-7363
Faculty Hall
University of Waterloo, Waterloo, Ontario
Wednesday, May 3, 2023**

8:45 a.m.	Open Symposium Portal
8:50	Welcome and Opening Remarks
9:00 - 9:20	Rohan Shorey, Chemical Engineering, Waterloo Unlocking the Potential of Lignin for Functional and Sustainable Material Solutions (Winner of 2022 IPR Award for Academic Excellence in Polymer Science/Engineering)
9:20 - 10:20	Industry Speaker: Dr. Jason Dockendorff, 3M. From Graduate School to Industry: Perspectives on Career Path and Some Interesting Discoveries and Projects Along the Way
10:20 – 10:45	<u>5-Min. Mini Presentations</u> 1) Zhe Huang Dual Effects of PVDF as a Binder Material on the Abnormal Voltage Behavior in the Initial Charge of Li ₂ S-based Li-S Battery 2) Xiguang Gao Coordination Polymers for Lithium-ion Batteries 3) Shahrzad Ghodrati Polymeric Sensing Materials for Energy Storage Devices 4) Naixin Zhao DOT-based Conductive Polymer via Direct Arylation 5) Andrew Stella Tailoring Novel Conductive Polymers for Flexible Toxic Gas Sensors
10:45 – 11:15	Coffee
11:15 – 11:35	Bhoomi Mavani Could Polymeric Materials Be Good Gas Detectors?

11:35-12:00	<p><u>5-Min. Mini Presentations</u></p> <p>6) Youchao Teng Biomass Hydrogels for Human Health Monitoring</p> <p>7) Kyle Pieters Stabilization of Biodegradable Polymer Dispersions in Aqueous Medium</p> <p>8) Rachel Blanchard Conversion of PET Bottle Waste to Activated Carbon for Dye Contaminated Wastewater Treatment</p> <p>9) Zahra Parsa Utilizing Advanced Oxidation Process (AOP) for the Degradation of Water-Soluble Polymers</p> <p>10) Dion Grobe Thiazole N-oxide Conjugated Polymers for Low Exciton Binding Organic Electronics</p>
12:00 - 1:00	Lunch E7 2357-2317
1:00 - 2:00	<p>Academic presenter: Dr. Mario Gauthier Emeritus Member of the IPR Controlled Architecture Polymers: What, Why and How?</p>
2:00 – 2:20	<p>Hunter Little Persistence Length of Poly(oligo(ethylene glycol) methyl ether methacrylate)s Determined by Pyrene Excimer Fluorescence.</p>
2:20 – 2:40	<p>Kristijan Lulic Persistence Length of Copolymers of Alkyl Methacrylates Probed by Pyrene Excimer Fluorescence</p>
2:40 - 3:00	<p>Azin Adibi , Chemical Engineering, Waterloo Development of biopolymer coating with high barrier performance based on enzymatic polysaccharide and natural rubber for paper-based packaging applications (Winner of the 2022 IPR Award for Academic Excellence in Polymer Science/Engineering)</p>
3:00 -3:20	<p>Ryan Lloyd Interactions Between DNA and Pyrene-Labeled Gemini Surfactant Probed by Fluorescence and Dynamic Light Scattering</p>
3:20-3:40	Coffee
3:40-4:00	<p>Franklin Frasca Conformation of Pyrene-Labeled Polyamines Established Through their Molecular Parameterization</p>
4:00-4:20	Sanjay Patel

Conformation of PAMAM Dendrimers Probed by Pyrene Excimer Fluorescence

4:20-4:40

Donghan Liu

Conformation of Poly(γ -Benzyl Glutamate) in Organic Solvents

4:45

Closing remarks

Rohan Shorey
Chemical Engineering
Waterloo

Unlocking the Potential of Lignin for Functional
and Sustainable Material Solutions

Winner of the 2023 IPR Award for Academic
Excellence in Polymer Science/Engineering

Unlocking the potential of lignin for functional and sustainable material solutions

Rohan Shorey, Tizazu H. Mekonnen*

Department of Chemical Engineering, Institute of Polymer Research, Waterloo Institute of
Nanotechnology, University of Waterloo, Waterloo, ON, Canada

Conventional polymers have revolutionized almost every aspect of modern life – from the clothes we wear to the materials utilized in packaging our food. However, the non-degradability of these polymers has led to significant plastic pollution concerns over the years. Growing environmental concerns about the production and disposal of synthetic and non-degradable polymers ^[1] are driving a shift toward the development of new materials based on renewable resources (e.g., starch, lignin, and cellulose polymers), as well as the design of biodegradable, multifunctional, and biocompatible polymers from natural macromolecule derivatives ^[2].

Lignin is the second most abundant natural biopolymer after cellulose, constituting anywhere from 18 to 35 wt.% of biomass, depending upon the feedstock type ^[3,4]. It is categorized as a biodegradable polymer as certain wood-rotting fungi, and some bacteria can depolymerize and mineralize it ^[5].

Lignin: An underutilized biopolymer

With an annual production of approximately 100 Mt/y ^[6], the global lignin biosphere availability is estimated to be 300 billion tonnes ^[7], out of which 50 to 70 million tonnes of lignin is paper and pulp industry sourced ^[6]. Currently, it is widely employed as a low-cost fuel in power and heat generation facilities ^[8] and a mere 2% is employed in the production of specialty chemicals (surfactants, dispersants, and adhesives production) ^[6]. In addition, a small percentage of lignin is also used as fillers in paint, ink varnishes, and elastomeric matrices ^[8].

Lignin is composed of three monolignol monomeric units: p-coumaryl, coniferyl, and sinapyl alcohols (as shown in **Figure 1**). Various types of lignin exist depending on the sourced wood feedstock and the employed extraction process. While kraft lignin and lignosulfonates are traditionally sourced from the paper industry, recent advances in biorefinery processes have produced sulfur-free organosolv lignin ^[6]. Furthermore, lignin can be produced from either soft or hardwood via dissolution or the hydrolysis of cellulose and hemicellulose at low pH resulting in an insoluble residual fraction ^[9]. Also, due to the aggressiveness of the extraction process, commercial lignin's molecular weight and polydispersity are highly dependent on the employed processes ^[6]. Overall, due to its abundance, sustainability, renewability, and presence of numerous functional groups that enable lignin modification, there is a significant interest in its utilization as a feedstock for bio-aromatic chemical syntheses, such as phenols and vanillin, and the production of bio-based polymeric materials for adhesives or composite applications ^[10].

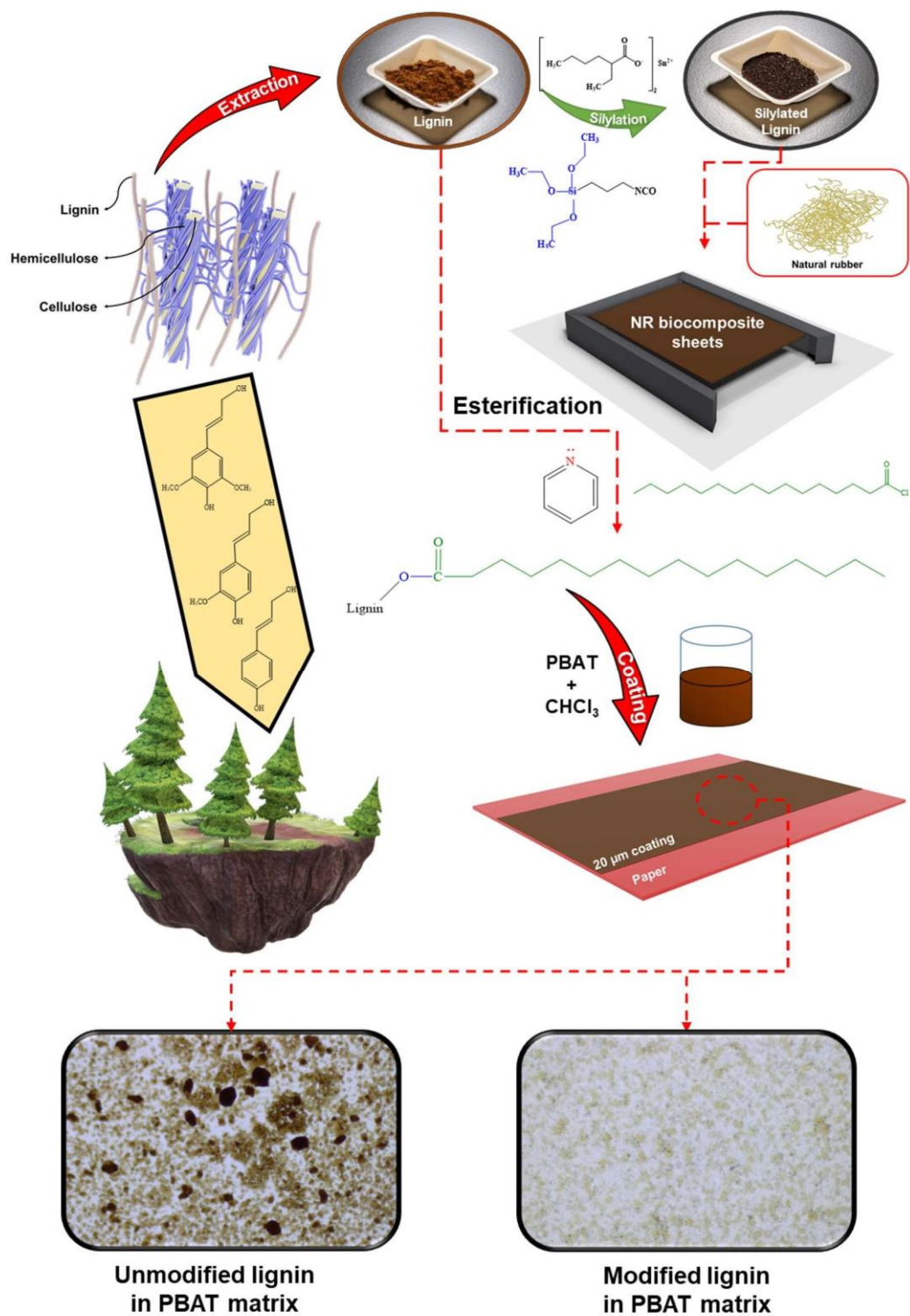


Figure 1. Graphical abstract representing the utilization of lignin in elastomers and packaging materials. The inherent limitations of lignin, such as thermal degradability, poor melt flow characteristics, incompatibility with hydrophobic polymeric matrices, a tendency to agglomerate in host matrices,

and variability in its chemical structure related to the feedstock source, limits its widescale utilization ^[11]. To effectively counter these limitations and valorize lignin, various lignin functionalization reactions have been reported in the literature ^[8].

Functionalization reactions

Lignin's structural modifications and functionalization processes range from biological to chemical, electrochemical, and photochemical processes. Over the years, various chemical modification reactions of lignin have been studied, including alkylation, methylation, amination, carboxylation, acylation, halogenation, nitration, hydrogenolysis, oxidation, reduction, sulfonation, esterification, silylation, and phosphorylation. Therefore, functionalized lignin specimens can be utilized in sustainable polymer applications ^[8,12-14].

Lignin incorporated elastomeric matrices

In native form, elastomers have a large free volume and exhibit poor performance. These limitations can be overcome by the use of appropriate reinforcing fillers and additives. While carbon black is the dominant filler of rubber products, concerns associated with the feedstock and production of carbon black in conjunction with its relatively higher density, and health and safety concerns associated with handling carbon black have led to an increasing interest in bio-sourced and sustainable fillers ^[15]. Lignin being widely available, bio-sourced, and economical can be employed as a filler for such elastomeric matrices.

Shorey et al. aimed at the incorporation of silylated kraft lignin into a natural rubber matrix through a solvent casting technique, as illustrated in **Figure 1** ^[12]. The proposed reaction mechanism was confirmed using viscosity evaluation, spectroscopic analysis, and dispersibility studies. It was observed that the modified lignin-based composite samples exhibited superior

tensile properties than their unmodified counterparts. For instance, the 5 wt.% modified lignin sample imparted a 44.4% increase in the tensile strength of the baseline NR. Overall, the silylation modification of lignin was a straightforward process that enhanced the reinforcing capability of lignin in natural rubber.

Packaging materials: Past, present, and future

Petroleum-sourced traditional polymers dominate the packing industry with their post-use disposal generating enormous amounts of plastic waste each year. To counter plastic pollution, efforts are directed towards renewable and biodegradable polymeric materials, shifting their production from petroleum feedstock to renewably sourced materials. Traditionally, the food packaging industry has benefited a lot from paper wraps and containers. However, the use of paper in some food packaging applications is limited due to inherent challenges, including poor moisture and oil barrier properties, and low wet tensile strength ^[13]. The application of polymer coatings on cellulosic paper could effectively address such inherent limitations ^[16].

For instance, polyethylene-coated cardboard is extensively used for hot beverage cups. Moreover, the use of synthetic polymers, such as poly(ethylene terephthalate), poly(ethylene), and poly(ethylene-co-vinyl alcohol), have led to significant environmental concerns associated with waste disposal, and in some cases safety (e.g, fluorocarbon) ^[16]. To mitigate the environmental damage caused by traditional plastics, the development of biodegradable, non-toxic, sustainable, and green polymeric packaging materials is receiving substantial attention ^[17].

A shift towards sustainable packaging alternatives

Amongst the available biodegradable polymers, poly(butylene adipate-co-terephthalate) (PBAT) is a fossil fuel-sourced compostable polymer that exhibits high flexibility and excellent moisture barrier ^[18]. This compostable polymer has been used in various applications ranging from hygiene products to biomedical fields and packaging materials, such as trash bags, packaging films, and food containers ^[19]. Although compostability is a desirable attribute, its mass applicability is restricted by its high cost, poor mechanical and thermomechanical properties ^[20]. To address these limitations, selected co-blends (e.g., thermoplastic starch) and bio-fillers (e.g., cellulose, lignin, chitin) are incorporated in the PBAT to reduce the production cost and improve its properties, while maintaining its biodegradability ^[18].

Lignin being a sustainable and abundant natural polyphenolic macromolecule, it is appealing to utilize it as an additive to PBAT and other sustainable polymers. With the growing interest in material sustainability, lignin valorization as a bio-filler or additive in biodegradable polymeric matrices is gaining significant attention.

This study aimed at the fabrication of lignin-incorporated PBAT paper coatings ^[13]. An esterification modification of the lignin was employed to substitute the abundant hydroxyl moieties with long aliphatic chains. The esterified lignin exhibited enhanced dispersibility in the non-polar PBAT paper coating formulations resulting in better wet tensile strength of the coated paper. With an increase in the concentration of esterified lignin in the coating formulations (up to 50 wt.%), appealing oxygen, oil, and water barrier properties were recorded. An increment in the coating thickness resulted in a further improvement in barrier properties, with the best barrier obtained using 60 μm thickness 50 wt.% esterified lignin-PBAT coatings. Overall, the fabricated paper coating films based on the esterified lignin and PBAT in this work demonstrated uniform surface morphology, better tensile properties, and remarkable barrier properties.

References:

- [1] J. R. Jambeck, R. Geyer, C. Wilcox, T. R. Siegler, M. Perryman, A. Andrady, R. Narayan, K. L. Law, *Science* (1979) 2015, 347, 768.
- [2] T. Mekonnen, P. Mussone, H. Khalil, D. Bressler, *J Mater Chem A Mater* 2013, 1, 13379.
- [3] F. S. Chakar, A. J. Ragauskas, "Review of current and future softwood kraft lignin process chemistry," *Industrial Crops and Products*, Elsevier, 1 September 2004.
- [4] R. C. PETERSEN, "The Chemical Composition of Wood," 1984, p. 57.
- [5] I. D. Reid, *Canadian Journal of Botany* 1995, 73, 1011.
- [6] D. S. Bajwa, G. Pourhashem, A. H. Ullah, S. G. Bajwa, *Ind Crops Prod* 2019, 139, 111526.
- [7] N. Smolarski, High-value opportunities for lignin: unlocking its potential, 2012.
- [8] *Chemical Modification, Properties, and Usage of Lignin*, Springer US, 2002.
- [9] C. Xu, F. Ferdosian, *Structure and Properties of Lignin*, 2017.
- [10] C. A. Cateto, M. F. Barreiro, A. E. Rodrigues, *Ind Crops Prod* 2008, 27, 168.
- [11] S. Sen, S. Patil, D. S. Argyropoulos, *Green Chemistry* 2015, 17, 4862.
- [12] R. Shorey, A. Gupta, T. H. Mekonnen, *Ind Crops Prod* 2021, 174, 114189.
- [13] R. Shorey, T. H. Mekonnen, *Int J Biol Macromol* 2022, 209, 472.
- [14] R. Shorey, T. H. Mekonnen, *Int J Biol Macromol* 2023, 230, 123143.
- [15] B. P. P. Chang, A. Gupta, R. Muthuraj, T. Mekonnen, *Green Chemistry* 2021.
- [16] K. Vaezi, G. Asadpour, S. H. Sharifi, *Polym Test* 2019, 80, 106080.
- [17] E. Divsalar, H. Tajik, M. Moradi, M. Forough, M. Lotfi, B. Kuswandi, *Int J Biol Macromol* 2018, 109, 1311.
- [18] F. V. Ferreira, L. S. Cividanes, R. F. Gouveia, L. M. F. Lona, *Polym Eng Sci* 2019, 59, E7.
- [19] K. Van De Velde, P. Kiekens, *Polym Test* 2002, 21, 433.
- [20] S.-J. Xiong, B. Pang, S.-J. Zhou, M.-K. Li, S. Yang, Y.-Y. Wang, Q. Shi, S.-F. Wang, T.-Q. Yuan, R.-C. Sun, *ACS Sustain Chem Eng* 2020, 8, 5338.

Dr. Jason Dockendorff
Industrial Presenter
3M Canada

From Graduate School to Industry:
Perspectives on Career Path and Some
Interesting Discoveries and Projects Along the
Way

From Graduate School to Industry: Perspectives on Career Path and Some Interesting Discoveries and Projects Along the Way

Dr. Jason Dokendorff

Much like polymer architectures, characteristics and synthetic methodologies, career paths can be described in a similar manner. They can be linear, cyclic or branched, they can be flexible or rigid, or they can even back-bite in some cases. A personal journey into academia, key findings during academic research, transition to industry, and some examples of industrial-based activities will be presented herein. Technical discussion will include findings related to arborescent copolymer synthesis and application for nanoparticle templating, particularly some newly discovered unimolecular nanomorphologies. Further, industrial production, troubleshooting activities, and product development in the areas of butyl rubber and coated abrasives will be reviewed. The discussion will also touch on lessons learned along the way and advice for career success.

Zhe Huang
Chemical Engineering
Waterloo

Dual Effects of PVDF as a Binder Material on
the Abnormal Voltage Behaviour in the Initial
Charge of Li_2S -Based Li-S Batteries

Dual Effects of PVDF as a Binder Material on the Abnormal Voltage Behavior in the Initial Charge of Li_2S -Based Li-S Battery

A Research Presentation for IPR Symposium
 Presented by: Zhe Huang
 Supervised by: Prof. Yuning Li
 Chemical Engineering (Nanotechnology)
 May 3rd, 2023



Research Backgrounds

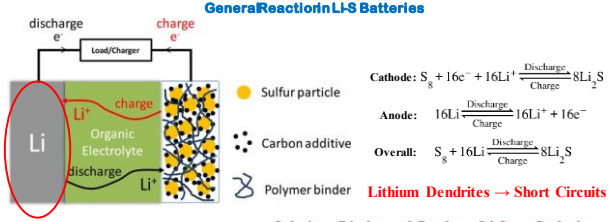


Figure 1 Schematic of Li-S batteries. **Solution: Discharged Product, Li_2S , as Cathode Compatible with non-metallic anodes, like graphite.**

Chem. Rev., 2014, 14(23): 11751–11787

PAGE 2



Research Backgrounds

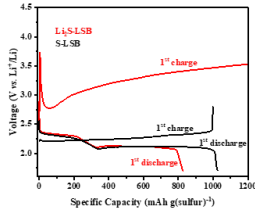


Figure 2 The first cyclic galvanostatic charge/discharge characteristics of typical Li_2S -LSB and S-LSB, where the specific capacities were normalized based on sulfur for a clearer comparison. The S-LSB data are adopted from literature.

ACS Appl. Mater. Interfaces 2021, 13, 20, 23932-3944

PAGE 3



Possible Reasons

- **High crystallinity of Li_2S .**
An antifluorite crystal structure with strong bond energy and high standard enthalpy of formation
- **The large size of Li_2S particles**
The smaller particles → the larger surface area, the shorter Li^+ diffusion length → the smaller overpotential.
- **Insulating $\text{LiOH}/\text{Li}_2\text{O}$ layer on the surface.**
Formed by absorbing moisture

Research Content

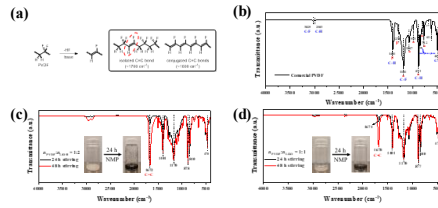


Figure 3 (a) Dehydrofluorination of PVDF in the presence of a base to form unsaturated C=C bonds. (b)–(d) FTIR spectra of commercial PVDF, PVDF reacted with LiOH ($\text{Li:F} = 1:1$) in NMP for 24 and 48 h, and PVDF reacted with Li_2O ($\text{Li:F} = 1:1$) in NMP for 24 and 48 h. Inserts in (c) and (d) show the reaction mixtures of PVDF and LiOH (b) and PVDF and Li_2O in NMP before and after reaction for 24 h.

Polymer 2000, 41 (5), 1685–1696.



Research Content

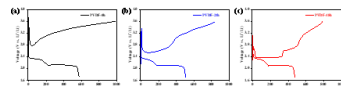
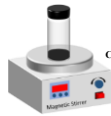


Figure 4 First charge/discharge curves of (a) PVDF-0h, (b) PVDF-24h, and (c) PVDF-48h. All the electrochemical tests were carried out at 0.1C ($1.0\text{C} = 1166\text{mA g}^{-1}$) with upper cut-off voltage of 3.6V .



$\text{Li}_2\text{S} + \text{Super P} + \text{PVDF}$ (7:2:1) in NMP, ground for 30 min. Constantly Stirred for 0 h, 12 h, and 48 h.

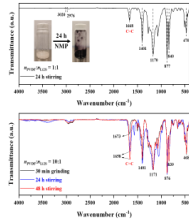


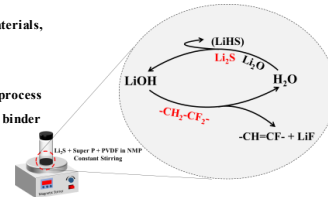
Figure 5 ATR-FTIR spectra of (a) PVDF treated with Li_2S (molar ratio $n_{\text{Li}_2\text{S}}:n_{\text{PVDF}}=1:1$) in anhydrous NMP by stirring for 24 h and (b) PVDF samples treated with Li_2S (molar ratio $n_{\text{Li}_2\text{S}}:n_{\text{PVDF}}=10:1$ or mass ratio $m_{\text{Li}_2\text{S}}:m_{\text{PVDF}}=70:10$) in anhydrous NMP by grinding for 30 min and stirring for 24 h and 48 h.



Conclusions

- PVDF can **remove $\text{LiOH}/\text{Li}_2\text{O}$ layer** on Li_2S particles, lowering the height of overpotential
- PVDF can also **consume Li_2S active materials**, resulting in a decreased capacity.

In all, PVDF shows dual effects on the 1st charge process of Li_2S -based Li-S batteries and it is not a stable binder material for its dehydrofluorination



Xiguang Gao
Chemical Engineering
Waterloo

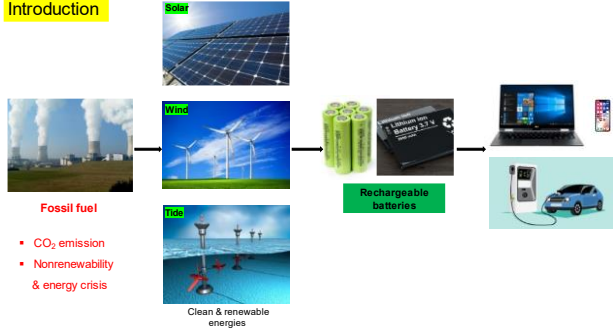
Coordination Polymers for Lithium-Ion Batteries

Coordination Polymers for Lithium-ion Batteries

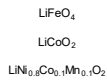
Xiguang Gao
 Postdoc, Department of Chemical Engineering
 Supervisor: Prof. Yuning Li
 May 3, 2023



Introduction

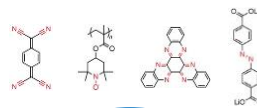


Current Li-ion cathode materials



- High cost (Ni, Co, Mn)
- Limited energy density
- Insufficient safety

Organic cathode materials

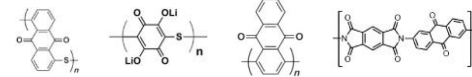


- Abundance in Nature (C, H, O, N)
- Tunable and diverse structures

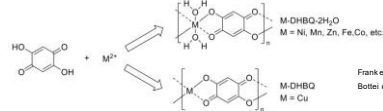
Quinone based organic cathode materials

- Challenge
- High solubility in organic electrolyte
- Fast capacity fading

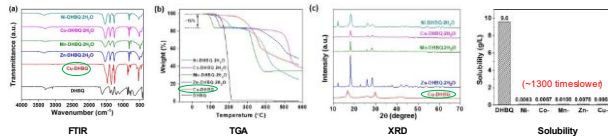
Conventional polymers



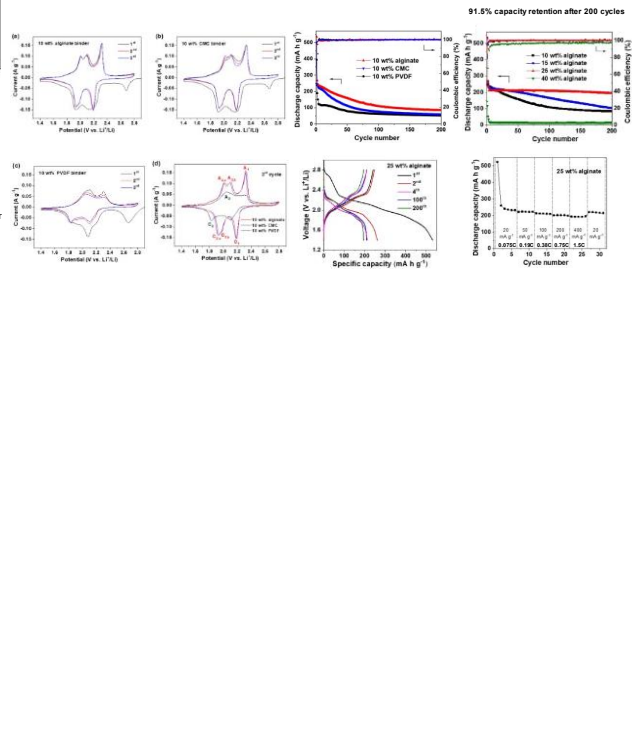
Coordination polymers



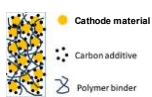
Frank et al. J. Am. Chem. Soc. 1950, 72, 1827-1829
 Bottei et al. J. Inorg. Nucl. Chem. 1966, 28, 1259-1264



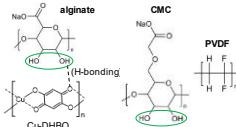
Optimization on the performance of Cu-DHBQ cathode using different types and amounts of binders



Structure of electrode film



Influence of polymer binder



- Stronger adhesive strength of alginate and CMC binders than PVDF binder
- Stronger interaction between alginate (or CMC binder) and CuDHBQ due to hydrogen-bonding

Shahrzad Ghodrati
Chemical Engineering
Waterloo

Polymeric Sensing Materials for Energy
Storage Devices

Polymeric Sensing Materials for Energy Storage Devices

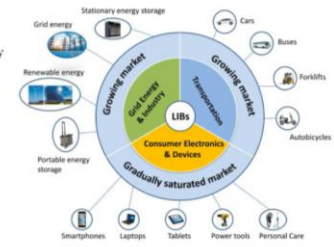
Shahrzad Ghodrati and Alexander Penlidis

Department of Chemical Engineering
University of Waterloo

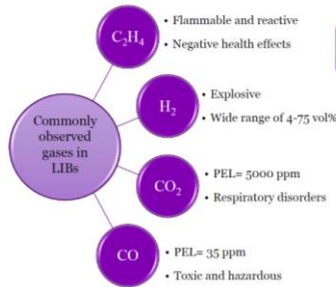


Motivation

- ❑ Lithium-ion batteries (LIBs) are a type of energy storage device becoming increasingly popular.
- ❑ However, gas evolution in LIBs poses a problem regarding safety (and battery cell performance).
- ❑ Gas evolution originates from the degradation of battery materials.
- ❑ Gases evolved can be hazardous in differing ways.



PAGE 2 <https://doi.org/10.1007/s41918-018-0022-z>

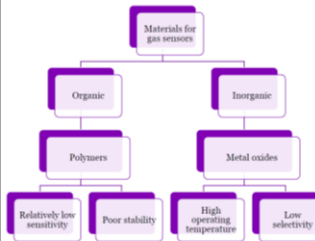


PEL: Permissible Exposure Limit

PAGE 3

Objective: To develop sensing materials for the detection of target analytes which are:

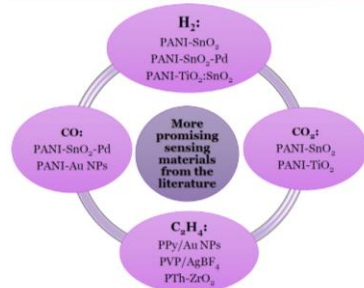
- operational at room temperature
- inexpensive and relatively easy to synthesize
- detectors of ppm levels of target gases



➤ The combination of organic and inorganic materials has been proposed to overcome the drawbacks of single inorganic or organic sensors.

➤ Optimal sensing material(s) can then be deposited on a sensor for its interaction with the target gas analyte to produce a signal.

PAGE 4



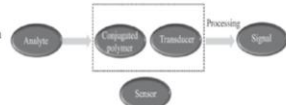
PANI: polyaniline, PPy: polypyrrole, PTh: polythiophene, PVP: polyvinylpyrrolidone
NPs: nanoparticles

- Important sensing characteristics for sensor performance evaluation: sensitivity, selectivity, stability (and operating temperature).
- **Sensitivity:** The lowest detectable limit of an analyte.
- **Selectivity:** The ability of a sensor to detect more of a specific analyte in the presence of other interferent gases.
- **Stability:** Reusability of the sensing material and how effective it is after ageing.

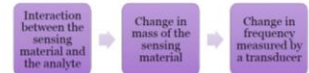
PAGE 5

MEMS Sensors (Micro-electro-mechanical systems)

- MEMS-based sensors are playing a leading role in detecting low concentrations of hazardous gases.
- Superior properties: small size, lightweight, high precision, portability, low power consumption, low cost, real-time measurement of analytes.
- A mass-based miniature sensor that requires a very small amount of sensing material.



Giaccia-Boschi, Pizzol and Corradini, Section 1.1.1, "Key components of a sensor," in Organic Sensors-Materials and Applications, Int. Eng. Technol., 2016, p. 2.



PAGE 6

Naixin Zhao
Chemical Engineering
Waterloo

DOT-based Conductive Polymer via Direct Arylation

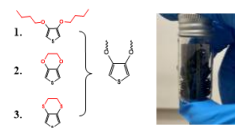
DOT-based Conductive Polymer via Direct Arylation

Presenter: Naixin Zhao
Supervisor: Dr. Yuning Li



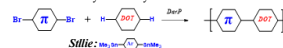
Introduction

DOT: 3,4-Di-alkylOxyThiophene derivatives



1. Linear (BOT) 2. Linear (EDOT) 3. O-analogue (EDTT)

DArP: Direct Arylation Polymerization



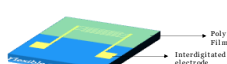
Substituent: $-Me, -Et, -iPr, -nBu, -OMe, -OEt, -OPh$

- Highlights:**
- DArP method eliminate use of toxic organotin side chain (**Green Chemistry**)
 - Electron-rich DOT spacer co-polymerized with electron-withdrawing conjugated core (**Low Bandgap**)
 - High HOMO level (**stable p-doping complex**)

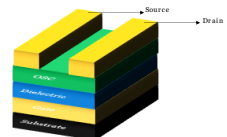
PAGE 2



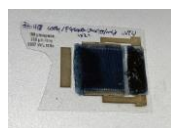
Temperature Sensor



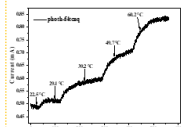
Resistor-based sensor



OTFT-based sensor



Polymer film coated on flexible substrate through blade-coating
Solution-doping by F4TCNQ

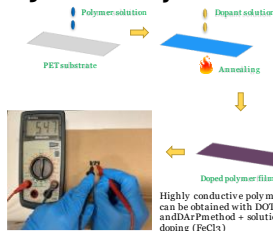


NTC sensing (~0.2% TCR)

PAGE 3



High Conductivity



Highly conductive polymer film can be obtained with DOT spacer and DArP method + solution doping (F4TCNQ)



Potential as flexible polymer electrode (diode)

PAGE 4



Summary

- 3,4-position protected at donor unit enable DArP, eco-friendly method compared to traditional polymerization method
- Low bandgap polymer with electron withdrawing moiety enable stable doping complex
- Good mobility/conductivity after doping, enable temperature sensing and organic electrode application

Thanks!

PRESENTATION TITLE

PAGE 5




Andrew Stella
Chemical Engineering
Waterloo



Tailoring Novel Conductive Polymers for
Flexible Toxic Gas Sensors

TAILORING NOVEL CONDUCTIVE POLYMERS FOR FLEXIBLE TOXIC GAS SENSORS

Andrew Stella,
PEML
Chemical Engineering



UNIVERSITY OF WATERLOO FACULTY OF ENGINEERING

modified from <https://www.cpsc.gov/safely/first-aid/first-aid-the-accident/>

Hierarchy of Controls

- Elimination
- Substitution
- Engineering
- Administrative
- PPE

- Goal: warm zone sensing for first responders

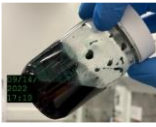
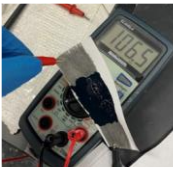
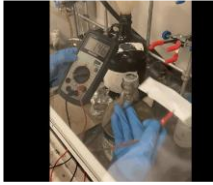
IPR: May 2023 - AIS PAGE 2

UNIVERSITY OF WATERLOO FACULTY OF ENGINEERING

Gas sensing

*c1ccc(cc1)C(=O)O.O=C(O)c1ccc(cc1)O>>[O=C(O)c1ccc(cc1)O]n2ccc(cc2)c3ccc(cc3)C(=O)O

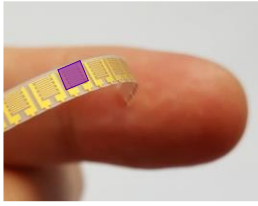
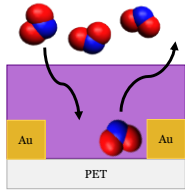
Chemical reaction showing the synthesis of a polymer with Au nanoparticles.

IPR: May 2023 - AIS PAGE 3

UNIVERSITY OF WATERLOO FACULTY OF ENGINEERING

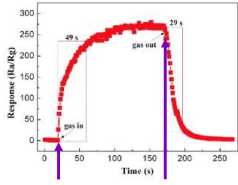
Sensor lag

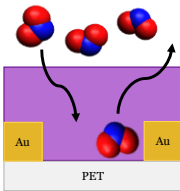
IPR: May 2023 - AIS PAGE 4

UNIVERSITY OF WATERLOO FACULTY OF ENGINEERING

Sensor lag



Highly Sensitive Acetone Gas Sensor Based on Ag@Pt Nanoparticles Decorated MnPc/Co Nanosheets Composite

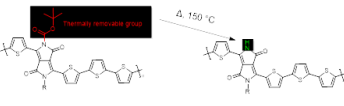


IPR: May 2023 - AIS PAGE 5



UNIVERSITY OF WATERLOO FACULTY OF ENGINEERING

Current work

- We use DPP, the "Ferrari Red" pigment, to make robust conductive polymers
- Use thermally removable groups to improve sensor response & recovery times



4, 150 °C

IPR: May 2023 - AIS PAGE 6

UNIVERSITY OF WATERLOO FACULTY OF ENGINEERING

Bhoomi Mavani
Chemical Engineering
Waterloo

Could Polymeric Materials Be Good Gas Detectors?

Could Polymeric Materials Be Good Gas Detectors?

Bhoomi Mavani and Alexander Penlidis

**Institute for Polymer Research, Department of Chemical Engineering,
University of Waterloo**

With the fast-paced growing technology and industrialization, the generation and emission of gas analytes like volatile organic compounds (VOCs), greenhouse gases (GHG), NO_x, SO_x, etc. have increased tremendously. These gases are released from various sources like the burning of fossil fuels, landfills, power generation, chemical industries and manufacturing plants, forest fires, mining activities, etc. Short-term and long-term exposure to these (often toxic) analytes can have harmful health implications for human beings. The effect of these analytes on other living organisms and the environment cannot be underestimated. Therefore, there is an urgent need to design and develop a high-performance portable/wearable gas sensor for the detection and monitoring of gas analytes both in air and aqueous media. Apart from environmental monitoring, gas sensors can also be used for medical diagnosis, safety and security (municipalities and urban environments), agricultural applications, and food quality monitoring.

Traditionally, these analytes have been dominantly monitored using analytical sampling techniques (like gas chromatography (GC), Infrared spectrometry, and Raman spectrometry), or electrochemical devices. The traditional techniques and devices may be accurate but are bulky, expensive, require a trained person to test and understand the results, and are relatively time-consuming. These sensors are expensive and usually operate at elevated temperature levels, prone to baseline drift and of shorter lifespans.

A sensor is a device that is capable of transforming information about the interaction between the analyte and sensing material into a measurable signal. A typical sensor consists of a sensing material (for interaction and detection of the analyte) and a transducer (for identifying the change in some property and converting it into a measurable signal). Sensors can be based on measuring different properties of the sensing material such as a change in mass, resistance or conductivity, and frequency. The sensing layer in a chemical sensor can be an organic sensing material (like polymeric materials) or an inorganic sensing material (like metal oxides). Important sensing characteristics to evaluate for sensor performance are LOD (limit of detection), response and recovery times, while those for sensing materials are sensitivity, selectivity, and stability.

Semiconductor metal oxides have been predominantly employed as sensing materials by most researchers in the literature. Some common metal oxides used for gas detection include, e.g., TiO₂ [1], ZnO [2], WO₃ [3], etc. They display enhanced sensitivity and low LOD but poor selectivity, low stability and are expensive. Typically, metal oxides are operated at elevated temperatures (like 300 C-500 C), thus requiring a heating source (within the sensor, making the sensor bulkier), consequently leading to stability issues and baseline drift. Another class of sensing material is polymers (often conducting). Common polymeric materials used for gas detection are polyaniline (PANI) [4], polypyrrole (PPy) [5], polythiophenes (PTh) [6], etc. They can be tailored for a specific target analyte by incorporating small amounts of dopants (like metals or metal oxides, and acids), addition of side chains, or modifying synthesis procedures. A major advantage of polymeric sensing material is room temperature detection, which eliminates the requirement for a heating source. Additionally, room temperature operation of polymeric materials helps with stability issues.

This research focuses mainly on the design and evaluation of polymeric gas sensing materials for indoor and outdoor detection of (toxic) analytes. Analytes are the ones mentioned above but may also include other chemicals (e.g., methane, ethylene, chemical warfare gases, etc.). If a specific analyte is a target, the analyte can be studied alone or with other “interferent” analytes. Often, if an analyte is too unsafe for a specific testing environment, then a “simulant” or “surrogate” may be studied. Analytes have to be detected somehow and in very small quantities (ppm).

A sensing material can be designed based on a systematic approach, meaning selecting materials based on their chemical nature, potential sensing mechanism and potential interaction with the target analyte. The most important factors to be considered while designing polymeric sensing materials are the target analyte, sensor constraints (i.e., type of sensor transducer, sensor application temperature, reusability, cost, energy requirements, etc.) and potential interactions between the analyte and sensing material. In the next step, one can select the potential dopants to characterize important sensing characteristics

One can use basic chemistry principles to check if a target analyte and potential detector polymer backbone possess appropriate functional groups that may create a certain affinity between the two parties. This affinity will be the first indication of whether the two molecules ‘like’ each other (based on primary and secondary mechanisms [7]). For instance, these mechanisms may involve the formation of hydrogen bonding, electron donor-acceptor compounds, Lewis acids and bases, and other steric considerations. This can be complemented by solubility considerations as well, since in any interaction between a polymer and an analyte, the polymer may get swollen by the analyte. Of course, other factors may include porosity and free volume or diffusion. That way, one can start with a list of potential detector polymers for a specific analyte of interest. Hence, we have established the potential polymer backbones for a particular target analyte. The next step will be to enrich the list of polymers with combinations of polymers and dopants which could be metals, metal oxides, acids, etc. Therefore, at this point one can analyse and evaluate potential polymeric sensing materials for their important gas sensing characteristics, such as sensitivity, selectivity, and stability. This thinking leading to the design/selection process along with representative examples will be illustrated at the time of the IPR conference.

References

- [1] S.-W. Lee, N. Takahara, S. Korposh, D.-H. Yang, K. Toko and T. Kunitake, "Nanoassembled Thin Film Gas Sensors. III. Sensitive Detection of Amine Odors Using TiO₂/Poly (acrylic acid) Ultrathin Film Quartz Crystal Microbalance Sensors," *Analytical Chemistry* 82, pp. 2228-2236, 2010
- [2] L. Wang, S. Wang, M. Xu, X. Hu, H. Zhang, Y. Wang and W. Huang, "A Au-functionalized ZnO nanowire gas sensor for detection of benzene and toluene," *Physical Chemistry Chemical Physics* 15, no. 40, pp. 17179-17186, 2013b
- [3] M.-T. Ke, M.-T. Lee, C.-Y. Lee and L.-M. Fu, "A MEMS-based benzene gas sensor with a self-heating WO₃ sensing layer," *Sensors* 9, no. 4, pp. 2895-2906, 2009
- [4] K. M. E. Stewart, N. M. McManus, E. Abdel-Rahman and A. Penlidis, "Doped polyaniline for the detection of formaldehyde," *Journal of Macromolecular Science*, vol. part A 49, pp. 1-6, 2012
- [5] A. J. Scott, N. Majdabadifarahani, K. M. Stewart, T. A. Duever and A. Penlidis, "Straightforward Synthesis and Evaluation of Polymeric Sensing Materials for Acetone Detection," *Macromolecular Reaction Engineering*, p. 2000004, 2020.
- [6] S. Bai, K. Zhang, J. Sun, D. Zhang, R. Luo, D. Li and C. Liu, "Polythiophene-WO₃ hybrid architectures for low-temperature H₂S detection," *Sensors and Actuators B: Chemical*, vol. 197, pp. 142-148, 2014
- [7] K. Stewart and A. Penlidis, "Designing polymeric sensing materials: what are we doing wrong?," *Polymers for Advanced Technologies*, vol. 133, no. 42, pp. 319-344, 2016

Youchao Teng
Chemical Engineering
Waterloo

Biomass Hydrogels for Human Health Monitoring

Biomass hydrogels for human health monitoring

Youchao Teng
 Supervisor: Yimin Wu & Michael Tam
 Department of Mechanical and Mechatronics Engineering
 Waterloo Institute for Nanotechnology
 University of Waterloo



Background

Most of the Wearables Market Today



Challenge

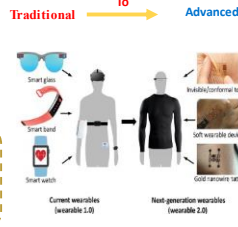
- Bulky sensing component
- Single stimuli-responsive function
- Energy supply devices requiring frequent charging
- Lack of precision, intimate skin interface frustrates reliable collection of clinical quality data

<https://www.time.com/3326576/neveroffline>
<https://mobiofi.infotech.com/resources/blog/wearabletechnology-in-healthcare> PAGE 2



Background

Current Medical Diagnosis



Challenge

- Blood analysis in centralized laboratories lack the real-time tracking.
- Painful skin invasive healthcare monitoring make infants and elder people uncomfortable.

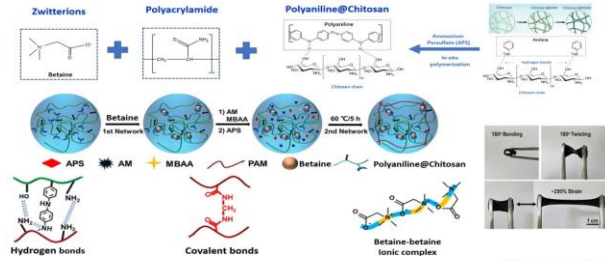
Y. Ling, et al. *Advanced Materials*, 2020, 32, 1904664.
 H. Lee, et al. *Nature nanotechnology*, 2016, 11, 566-572.

PAGE 3



Research Methodologies

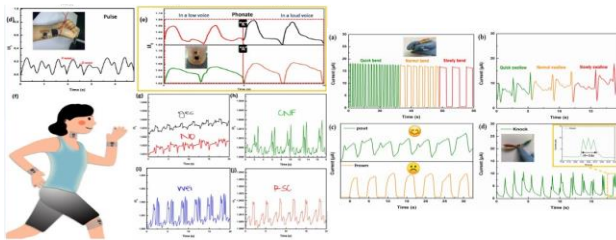
Accomplished Result



PAGE 5



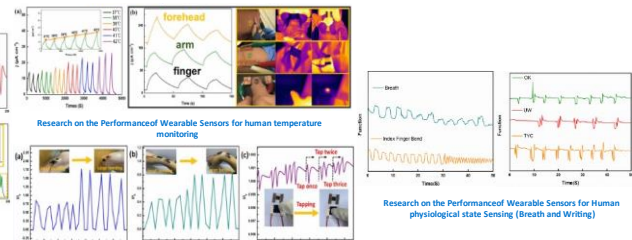
Accomplished Result



PAGE 6



Accomplished Result



PAGE 7



Thank you for your attention!



Kyle Pieters
Chemical Engineering
Waterloo

Stabilization of Biodegradable Polymer Dispersions in Aqueous Medium

STABILIZATION OF BIODEGRADABLE POLYMER DISPERSIONS IN AQUEOUS MEDIUM

Kyle Pieters
 Supervised by Professor Ezzatu Mekonnen
 May 2023

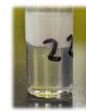


1

Background



Growing Bans and Concern over Single use Plastics



Many biodegradable alternatives not stable in aqueous medium

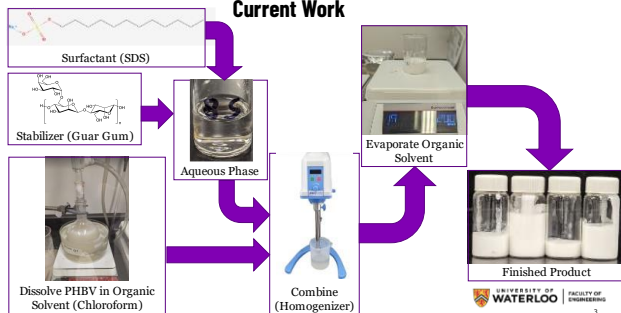


Investigate stabilizing waterborne dispersions of biodegradable plastics



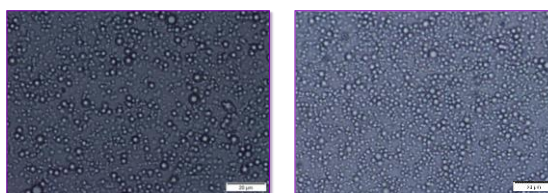
2

Current Work



3

Results (1/2)

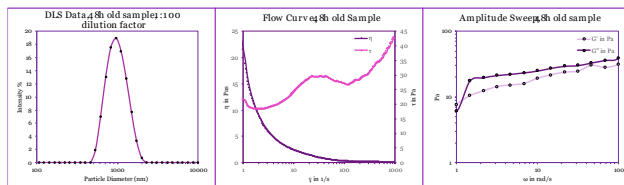


48h (left) vs 3 week (right) elapsed time. Both samples 1:10 dilution factor. Note similar particle sizes



4

Results (2/2)



5

Future Work

- Improve Coatability
- Remove Chloroform
- Pickering Emulsion



Conclusion

- >1 Month Stability
- >10% Solids Content
- Good Rheological Properties for Coating



6

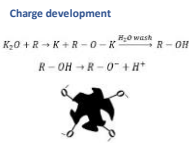
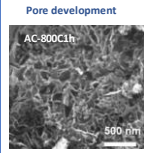
Rachel Blanchard
Chemical Engineering
Waterloo

Conversion of PET Bottle Waste to Activated
Carbon for Dye Contaminated Wastewater
Treatment

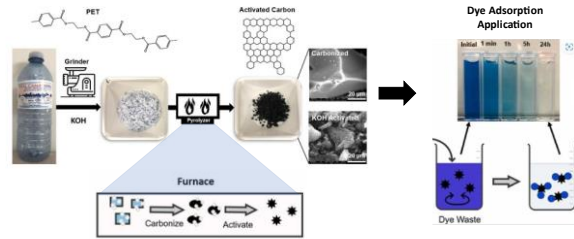


Activation Conditions	Yield (%)	BET Surface Area (m ² /g)*	Zeta Potential (mV)*
600°C 1h (no KOH)	17.34 ± 1.0	407.50 ± 0.87*	-34.5 ± 1.6*
700°C 1h	29.6 ± 2.9	625.63 ± 0.70*	-35.3 ± 1.6*
700°C 2h	27.4 ± 2.5	816.48 ± 3.85*	-34.1 ± 1.2*
800°C 1h	25.4 ± 2.5	1124.07 ± 1.66*	-39.6 ± 0.7*
800°C 2h	21.8 ± 2.1	1214.74 ± 4.90*	-39.9 ± 1.8*

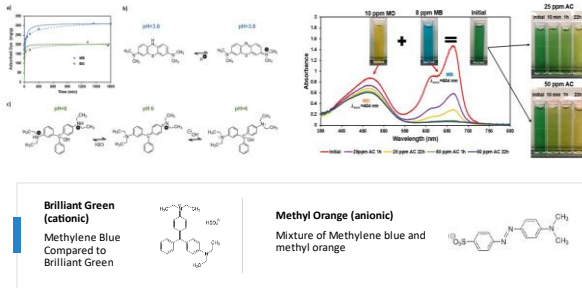
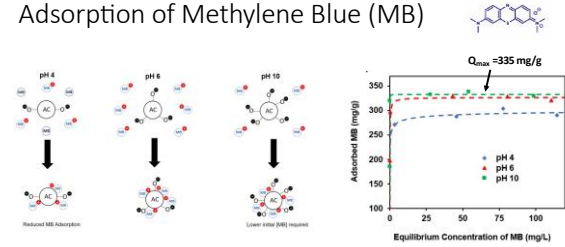
Key Adsorbent Properties



Conversion of PET Bottles to Activated Carbon

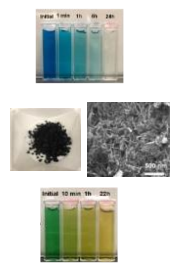


Adsorption of Methylene Blue (MB)



Conclusions

- PET produces AC with properties ideal for adsorption of cationic dyes
- Preliminary optimization conditions: 800°C 1h
 - Surface area of 1124 m²/g
 - Yield of 25%
 - Zeta potential of -40mV
 - MB adsorption of 335 mg/g
- Adsorption depends on dye characteristic and pH



Zahra Parsa
Chemical Engineering
Toronto

Utilizing Advanced Oxidation Process (AOP) for the Degradation of Water-Soluble Polymers

Utilizing an Advanced Oxidation Process (AOP) for the Degradation of Water - soluble Polymers

Zahra Parsa, Ramdhane Dhib, and Mehrab Mehrvar

45th ANNUAL SYMPOSIUM ON POLYMER SCIENCE/ENGINEERING 2023



May 3, 2023

Degradation of Polyvinyl alcohol (PVA) in the UV/H₂O₂ process

PVA is a synthetic water-soluble polymer with alcohol groups in its structure.

Problem:

- ✓ Global industrial consumption is over one million tons per year (+ 3.5% per year)
- ✓ High consumption causes producing a considerable amount of wastewater containing PVA,
- ✓ Toxic. Cause oxygen depletion in water sources, BOD₅/COD < 0.1,
- ✓ Couldn't be treated by conventional treatment methods.



Figure 1: The molecular structure of vinyl alcohol (C₂H₄O)

Table 1. Process variables and process responses in degradation of PVA in UV/H₂O₂ photoreactor and the analytical method for analyzing each process response.

Process variable	
Inlet PVA concentration (mg/L)	
Inlet H ₂ O ₂ concentration (mg/L)	
Feed flowrate (mL/min)	
Process Response	
% TOC removal	Combustion
% COD removal	Closed reflux colorimetric
BOD ₅ /COD	Respirometry/ Closed reflux colorimetric

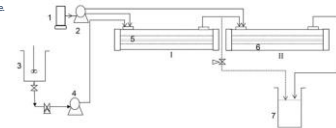


Figure 2. Schematic diagram of the continuous UV/H₂O₂ system. I, II Photoreactors. 1. H₂O₂ storage. 2. Multichannel peristaltic pumps. 3. Feed tank. 4. Feed peristaltic pump. 5. UV lamp. 6. Reaction zone. 7. Effluent tank.

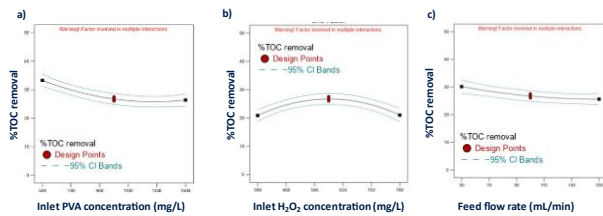


Figure 3. The individual effect of a) inlet PVA concentration (mg/L), b) inlet H₂O₂ concentration (mg/L), and c) feed flow rate (mL/min) on the %TOC removal in the UV/H₂O₂ photoreactor while other variables are kept constant at their central value.

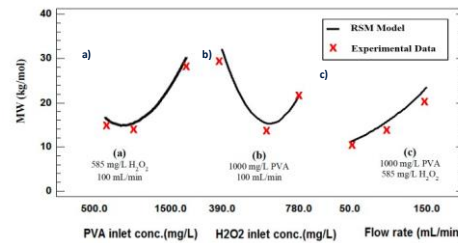


Figure 4. The individual effect of a) inlet PVA concentration (mg/L), b) inlet H₂O₂ concentration (mg/L), and c) feed flow rate (mL/min) on the PVA molecular weight (kg/mol) in the UV/H₂O₂ photoreactor while other variables are kept constant at their central value.

Conclusions

- The low-biodegradability property of PVA-contained wastewater was proved through preliminary tests.
- TOC and COD removal from the wastewater up to 30.71% and 36.19%, respectively, were achieved while the process operated at experimental operation ranges.
- The significant effect of process variables and their interactions on the process responses was observed.
- The biodegradability of PVA-contained wastewater was enhanced successfully using the UV/H₂O₂ process up to BOD₅/COD=0.57 while the process was operating at experimental operation ranges.
- ±10% of predicted process responses at suggested optimum operating conditions were achieved.

Utilizing an Advanced Oxidation Process (AOP) for the Degradation of Water - soluble Polymers

Zahra Parsa, Ramdhane Dhib, and Mehrab Mehrvar

45th ANNUAL SYMPOSIUM ON POLYMER SCIENCE/ENGINEERING 2023



May 3, 2023

Dion Grobe
Chemistry
Waterloo

Thiazole N-Oxide Conjugated Polymers for Low Exciton Binding Organic Electronics

Dr. Mario Gauthier
Academic Speaker
Emeritus Member of the IPR

Controlled Architecture Polymers: What, Why, and How

CONTROLLED ARCHITECTURE POLYMERS: WHAT, WHY, AND HOW?

Mario Gauthier

Institute for Polymer Research and Waterloo Institute for Nanotechnology, Department of Chemistry, University of Waterloo, 200 University Ave. West, Waterloo, ON N2L 3G1, Canada

For well over 50 years, but particularly with the expansion of nanotechnology, there has been ever-increasing interest in controlled architecture polymers. While research in that area initially focused on simple atactic block copolymers and star-branched polymers, it meanwhile expanded considerably to include more complex architectures. This now includes stereo-block, miktoarm star and star-block copolymers, but also more intriguing structures such as H-shaped, dumbbell and dendritic polymers, to name a few, whereby the characteristics of the molecules (building block composition, size uniformity, and placement) can be controlled more or less accurately. Many of these materials have been useful in understanding the physical properties of polymers, such as the influence of branching on melt flow characteristics relevant to processing, phase separation in polymers on the nanometer scale, or simply as curiosities aimed at demonstrating synthetic techniques. Selected examples from our laboratory will be used to illustrate how the characteristics of controlled architecture polymers (in particular arborescent and other dendritic polymers) can be varied, with the goal of producing materials with tailored properties, suitable for applications in different areas including materials science and the biomedical field.

Hunter Little
Chemistry
Waterloo

Persistence Length of Poly(oligo(ethylene glycol) methyl ether methacrylate)s Determined by Pyrene Excimer Fluorescence

Persistence Length of Poly(oligo(ethylene glycol) methyl ether methacrylate)s Determined by Pyrene Excimer Fluorescence

Hunter Little, Janine Thoma, Raymond Yeung, Adrianna D'Sa, and Jean Duhamel

Institute for Polymer Research, Waterloo Institute for Nanotechnology, Department of Chemistry, University of Waterloo, ON, N2L 3G1, Canada

INTRODUCTION

The mechanical properties of polymer materials are best understood from the macroscopic level. How quickly a polymer can deform under stress is dictated by the ability of individual chains to bend.¹ The flexibility of polymer chains is often quantified by the persistence length (l_p) also described as the distance over which orientation persists along the chain contour. Polymers with a larger l_p exhibit a more extended conformation than polymers with smaller l_p and are therefore viewed as intrinsically stiffer polymers.^{2,3} This effect is illustrated in Figure 1 where each chain is made of a same number of 24 beads, but where the chain on the left with a short l_p equivalent to 2 beads has a much more coiled conformation than the chain on the right with a longer l_p of 4 beads.

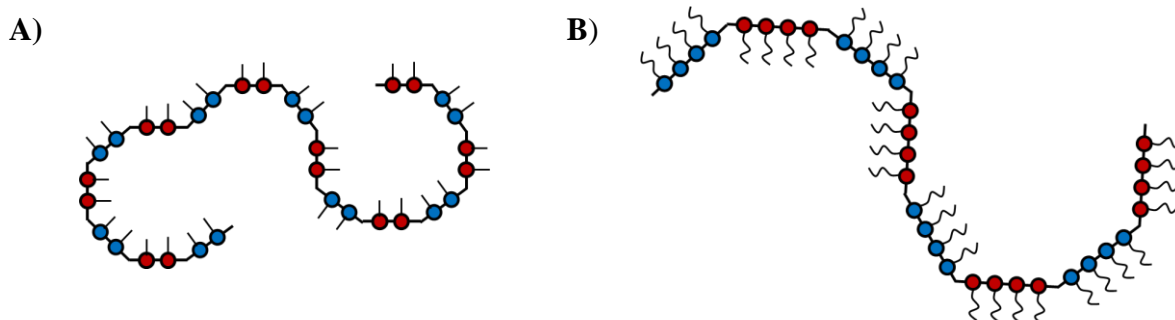


Figure 1. Depiction of polymers with (A) a small and (B) a large persistence length.

Due to the challenges of measuring l_p , it is more often encountered as a theoretical parameter used to describe the flexibility of a polymer. Traditionally, l_p is determined using intrinsic viscosity, scattering techniques,¹ or GPC experiments² which relate l_p to the radius of gyration or the intrinsic viscosity, respectively. Though these techniques represent the common methodology currently in place, they have severe limitations to their use. Scattering techniques require multiple samples of monodisperse polymers,⁴ while GPC instruments require stringent calibration and no interaction between the polymer and packing material⁵ and are often limited to running a single solvent that may not be compatible with the polymer of interest. Thus, alternative methods which can be used as complementary techniques should be sought in order to fulfil three principal requirements. First, the technique should be compatible with polymers of broad molecular weight distributions; second, the technique should be easy to apply in a wide range of solvents of different polarities and viscosities, and finally, the technique should be capable of exclusively probing the polymer backbone without interference from the side-groups.

An excellent technique for probing the structure of a polymer backbone is pyrene excimer fluorescence (PEF). The fluorophore pyrene is widely used due to its long lifetime, high quantum yield, and especially for its ability to form excimer.⁶ Excimer is formed when an excited pyrene encounters a ground-state pyrene during its lifetime resulting in a chromatically and temporally

distinct emission from that of the pyrene monomer.⁶ The beauty of PEF is that, when pyrenyl-moieties are attached onto a macromolecule, PEF can only occur through direct contact between an excited and ground-state pyrenyl label without energy hopping.⁶ Thus, PEF is solely controlled by the diffusion of the polymer backbone. What's more, since the monomer and excimer emissions are chromatically and temporally distinct, the process of PEF can be monitored using time-resolved fluorescence (TRF) which can separate the different pyrene species contributing to PEF based on their unique temporal signatures.

The TRF decays of the pyrene monomer and excimer are analyzed globally according to the fluorescence blob model (FBM). The FBM assumes that the macromolecule has been randomly labelled with pyrene, which distributes itself among the *blobs* according to a Poisson distribution, where a *blob* is the volume probed by a pyrenyl label while it remains excited.⁷ In a display of mathematical magic, the FBM takes the TRF decays of polydisperse polymers that have been randomly labelled with pyrene and retrieves the absolute value of the number of structural units visible to the excited pyrene (N_{blob}).⁷ N_{blob} has been used frequently by the Duhamel lab to quantify the ability of a polymer to coil, with a highly flexible polymer having a larger N_{blob} —and thus more structural units visible to the excited pyrene—than a polymer with a low N_{blob} . Since l_p and N_{blob} both report on the flexibility of a polymer chain, the two parameters must in some way be related. The purpose of this study was to then use a series of pyrene-labelled polymeric bottle brushes (PBB) to relate N_{blob} to l_p . The PBBs in question were chosen to possess a methacrylate backbone and pyrene-butyl derivative to better correlate with a similar study where N_{blob} was used to calibrate the flexibility of a series of poly(alkyl methacrylate)s.⁸ The side-chains were chosen to be oligo(ethylene glycol) for its expected ability to improve the solubility of the PBBs in polar solvents such as the low viscosity acetone and the highly viscous dimethylsulfoxide (DMSO).

EXPERIMENTAL

A series of pyrene-labelled poly(oligo(ethylene glycol)methyl ether methacrylate)s (Py-PEG_nMA) with $n = 0-5, 9, 16, 19$ were prepared by free-radical polymerization using 1-pyrenebutyl methacrylate and the corresponding oligo(ethylene glycol)methyl ether methacrylate. Py-PEG₀MA, corresponding to poly(methyl methacrylate) and Py-PEG₁₉MA were prepared by Drs. Shiva Farhangi⁸ and Janine Thoma,⁹ respectively. The reaction scheme for the preparation of the Py-PEG_nMA constructs is shown in Figure 1. This yielded a total of 41 polymer constructs of varying pyrene contents.

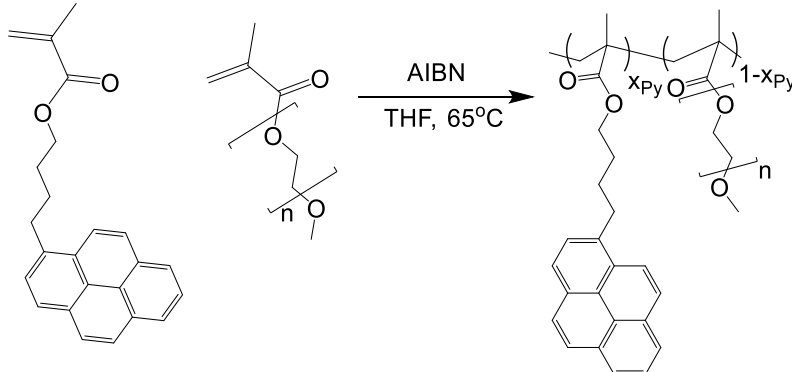


Figure 1. Reaction scheme for the preparation of the Py-PEG_nMA where $n = 0-5, 9, 16, 19$

Before acquiring the fluorescence decays, the Py-PEG_nMA were dissolved in the chosen solvent to a pyrene concentration of 2.5 μM , corresponding to a pyrene absorbance of 0.1 OD at 344 nm and a polymer concentration of ~ 5 mg/L, low enough to prevent intermolecular excimer

formation. Nitrogen was bubbled through the solution for 30 minutes in acetone, THF, toluene, and dioxane, or 45 minutes in DFM and DMSO, to remove dissolved oxygen, a known quencher of pyrene fluorescence. The fluorescence decays were analyzed using programs written in-house.

RESULTS AND DISCUSSION

The N_{blob} values determined by fitting the fluorescence decays of all 41 polymers in 6 solvents were plotted as a function of the molecular weight of a structural unit (MW_{SU}) in Figure 2A where two distinct regimes are noticed. N_{blob} reached a plateau and became independent of MW_{SU} for polymers with $MW_{\text{SU}} > 500$ g/mol. This effect is due to the complete extension of the polymer backbone; once fully extended any subsequent increase in side-chain size does not affect the backbone conformation, and thus N_{blob} . Since the plateau region of Figure 2A is independent of MW_{SU} , it is exclusively governed by solvent viscosity. The N_{blob} values of the Py-PEG₁₆MA and Py-PEG₁₉MA samples were plotted as a function of η^{-1} in Figure 2B, which yielded a straight line. The N_{blob} values defined by this line for the longest side-chains are expected to be identical to those for polymers with infinitely long side chains, and are therefore described as $N_{\text{blob},\infty}$.

As side chain size decreases, steric hindrance decreases and the backbone adopts a more coiled conformation resulting in N_{blob} increasing with decreasing MW_{SU} for $MW_{\text{SU}} < 500$ g/mol. This could be described in terms of a bending function.¹⁰ Equation 1 was derived where the first bracketed term describes the plateau value ($N_{\text{blob},\infty}$) and the second bracketed term corresponds to the bending function.

$$N_{\text{blob}}^{\text{theo}} = \left(10.1 \pm 0.4 + \frac{1.4 \pm 0.3}{\eta} \right) \times \left(\exp(10.2 \pm 1.2) \times MW_{\text{SU}}^{-2.0 \pm 0.2} \times \eta^{-0.53 \pm 0.12} + 1 \right) \quad (1)$$

The theoretical N_{blob} ($N_{\text{blob}}^{\text{theo}}$) was well defined by only two parameters: the molecular weight of the structural unit and the solution viscosity. This suggests a certain universality whereby N_{blob} can be described in terms of a small number of select parameters for any polymer. Equation 1 was found to faithfully retrieve the expected N_{blob} as shown in Figure 2C, where data points for the plot of $N_{\text{blob}} \text{ vs } N_{\text{blob}}^{\text{theo}}$ were seen to perfectly cluster around the diagonal.

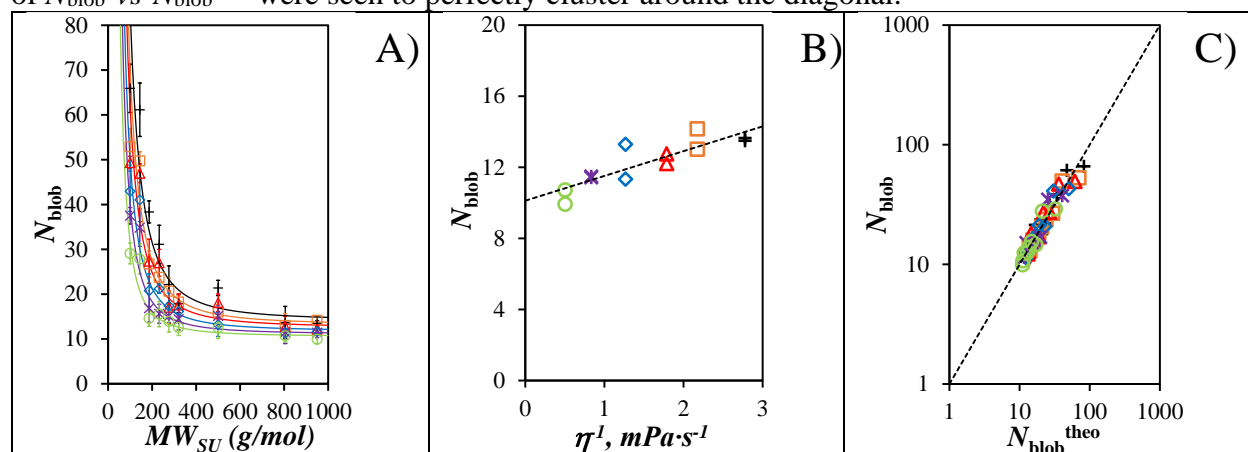


Figure 2. Plot of A) $\langle N_{\text{blob}} \rangle$ as a function of MW_{SU} with the lines representing the scaling law given by Equations 1, B) N_{blob} as a function of η^{-1} for the Py-PEG_nMA samples with $n = 16$ and 19, and C) N_{blob} as a function of $N_{\text{blob}}^{\text{theo}}$ with the black line indicating the 1:1 diagonal (Pearson correlation coefficient = 0.93). (+, $\eta = 0.36$ mPa.s) acetone, (\square , $\eta = 0.46$ mPa.s) THF, (\triangle , $\eta = 0.56$ mPa.s) toluene, (\diamond , $\eta = 0.79$ mPa.s) DMF, (\times , $\eta = 1.2$ mPa.s) dioxane, and (\circ , $\eta = 1.99$ mPa.s) DMSO.

Since N_{blob} responds to the flexibility of the polymer backbone, it must be related to the persistence length l_p . The Kratky-Porod Equation relates the mean squared end-to-end distance ($\langle r_{EE}^2 \rangle$) of a polymer chain to its l_p .¹¹ Adjusting the Kratky-Porod equation for the segment of chain contained within a *blob* yielded Equation 2, where b is the length of a monomer unit taken to be 0.25 nm¹² and $\langle r_{EE}^2 \rangle$ can be constrained by the size of a fully extended polymer chain, taken to be $(b \times N_{\text{blob},\infty})^2$.

$$\langle r_{EE}^2 \rangle_{\text{blob}} = 2l_p (b \times N_{\text{blob}}) - 2l_p^2 \left[1 - \exp\left(-\frac{b \times N_{\text{blob}}}{l_p}\right) \right] \quad (2)$$

Using both the experimental (N_{blob}) and theoretically predicted ($N_{\text{blob}}^{\text{theo}}$) values, l_p was extracted from Equation 2 and plotted as a function of the square of the number of atoms in a side-chain (N_S^2). These were plotted in acetone, THF, DMF, and dioxane, shown in Figure 3A-D. Though the experimental data points do show some scatter, they cluster to the dotted line representing the l_p values determined from $N_{\text{blob}}^{\text{theo}}$.

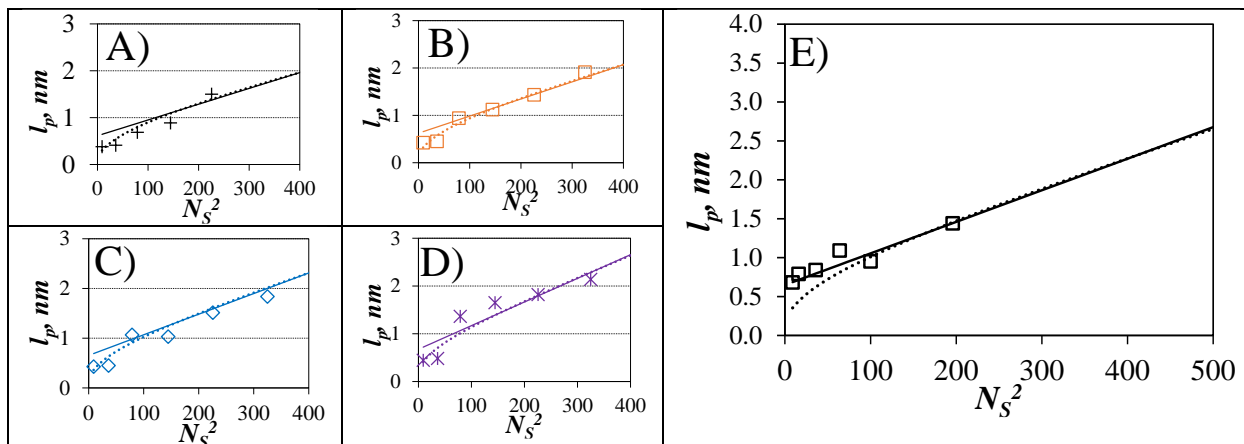


Figure 3. Plot of l_p as a function of N_S^2 for Py-PEG_nMA samples calculated with Equations 1 and 2 in A) (.....) acetone ($\eta = 0.36$ mPa.s), B) (.....) THF ($\eta = 0.46$ mPa.s), C) (.....) DMF ($\eta = 0.79$ mPa.s), D) (.....) dioxane ($\eta = 1.20$ mPa.s) and E) a hypothetical solvent of viscosity equal to 0.74 mPa.s. Solid lines represent the fit of the linear portion of the plot for N_S^2 values between 100 and 500 corresponding to N_S values between 10 and 22. l_p values obtained from the experimental $\langle N_{\text{blob}} \rangle$ obtained in (+) acetone, (□) THF, (◇) DMF, and (*) dioxane. (■) l_p values for a series of PAMA under θ -condition determined by viscometry and reported in Ref 3.

There are several important features to consider in Figure 3A-D. First is that the trends in l_p scale linearly with N_S^2 , validating Fredrickson's prediction regarding the scaling of l_p .¹³ The second feature of interest is that l_p appears to increase with increasing solvent viscosity. This is not unreasonable as PEF is itself a diffusion-controlled process. Molecular mechanics optimization was used to determine the $N_{\text{blob},\infty}$ for an unperturbed PMMA chain. This $N_{\text{blob},\infty}$ corresponded to a viscosity of 0.74 mPa.s, which represented conditions where PEF was no longer affected by solvent viscosity. Using Equations 1 and 2, an l_p -vs- N_S^2 curve for unperturbed Py-PEG_nMA was generated for a solvent viscosity of 0.74 mPa.s and is shown in Figure 3E with the linear portion of this curve taken to be between $100 < N_S^2 < 500$ and described by Equation 3.

$$l_p = 0.65 (\pm 0.01) + 4.06 (\pm 0.01) \times 10^{-3} \times N_S^2 \quad (3)$$

Plotted over the curve is the l_p values for a series of PAMAs obtained under θ -conditions.³ These values showed excellent agreement with the linear portion of the predicted curve described by Equation 3. Although Equation 3 is expected to remain valid for $N_S^2 < 500$, corresponding to polymers with side-chains shorter than 22 non-hydrogen atoms, this covers most commercially available PAMAs including poly(stearyl methacrylate). Therefore, Equation 3 provides a tool by which l_p could be predicted for the vast majority of linear PAMAs.

CONCLUSIONS

The persistence length is an often spoken-of parameter to quantify the flexibility of polymers, but due to stringent requirements of current methodology, namely intrinsic viscosity, scattering techniques, or GPC experiments, few scientists elect to measure it. This study demonstrates the feasibility of applying PEF to determine l_p for a series of Py-PEG_nMA. Since the FBM compartmentalizes the polymer into *blobs*, this analysis is perfectly viable for polydisperse polymers. It further fulfills the two requirements previously mentioned; PEF is perfectly suitable to any solvent the polymer can be dissolved into, and the short pyrene-butyl linker keeps the motion of the pyrene correlated to that of the backbone, meaning the side chains do not affect the measurement itself.

l_p predicted for the Py-PEG_nMA samples not only validated the theoretical predictions regarding how l_p scales as a function of side chain length, but were also found to accurately describe the l_p of PAMAs under θ -conditions. This implies that the structure of the polymer is more important for the determination of l_p than the chemical composition of the side chains. With the addition of PEF to the repertoire of methodologies for determining l_p , this useful parameter should no longer be relegated to a theoretical value but instead a widely tabulated, experimentally determined piece of information accessible to all polymer chemists.

REFERENCES

- (1) Kikuchi, M.; Nakano, R.; Jinbo, Y.; Saito, Y.; Ohno, S.; Togashi, D.; Enomoto, K.; Narumi, A.; Haba, O.; Kawaguchi, S. Graft Density Dependence of Main Chain Stiffness in Molecular Rod Brushes. *Macromolecules* **2015**, *48*, 5878–5886.
- (2) Mourey, T.; Le, K.; Bryan, T.; Zheng, S.; Bennett, G. Determining Persistence Length by Size-Exclusion Chromatography. *Polymer (Guildf)*. **2005**, *46*, 9033–9042.
- (3) Tricot, M. Chain Flexibility Parameter and Persistence Length of Various Poly(Methacrylic Acid Esters). *Macromolecules* **1986**, *19*, 1268–1270.
- (4) Rudin, A. *The Elements of Polymer Science & Engineering*; Elsevier Science & Technology Books, 1998.
- (5) Yekta, A.; Duhamel, J.; Adiwidjaja, H.; Brochard, P.; Winnik, M. A. Association Structure of Telechelic Associative Thickeners in Water. *Langmuir* **1993**, *9*, 881–883.
- (6) Duhamel, J. Global Analysis of Fluorescence Decays to Probe the Internal Dynamics of Fluorescently Labeled Macromolecules. *Langmuir* **2014**, *30*, 2307–2324.
- (7) Mathew, A. K.; Siu, H.; Duhamel, J. A Blob Model To Study Chain Folding by Fluorescence. *Macromolecules* **1999**, *32*, 7100–7108.
- (8) Farhangi, S.; Weiss, H.; Duhamel, J. Effect of Side-Chain Length on the Polymer Chain Dynamics of Poly(Alkyl Methacrylate)s in Solution. *Macromolecules* **2013**, *46*, 9738–9747.
- (9) Thoma, J. L.; Duhamel, J. Characterization of the Local Volume Probed by the Side-Chain Ends of Poly(Oligo(Ethylene Glycol) 1-Pyrenemethyl Ether Methacrylate) Bottle Brushes in Solution Using Pyrene Excimer Fluorescence. *Macromolecules* **2021**, *54*, 9341–9350.
- (10) Casier, R.; Duhamel, J. The Effect of Amino Acid Size on the Internal Dynamics and Conformational Freedom of Polypeptides. *Macromolecules* **2020**, *53*, 9811–9822.
- (11) Kratky, O.; Porod, G. Röntgenuntersuchung Gelöster Fadenmoleküle. *Recl. Trav. Chim* **1949**, *68*, 1106–1122.
- (12) Rathgeber, S.; Pakula, T.; Wilk, A.; Matyjaszewski, K.; Beers, K. L. On the Shape of Bottle-Brush Macromolecules: Systematic Variation of Architectural Parameters. *J. Chem. Phys.* **2005**, *122*, 164903.
- (13) Fredrickson, G. H. Surfactant-Induced Lyotropic Behavior of Flexible Polymer Solutions. *Macromolecules* **1993**, *26*, 2825–2831.

Kristijan Lulic
Chemistry
Waterloo

Persistence Length of Copolymers of Alkyl
Methacrylates Probed by Pyrene Excimer
Fluorescence

Persistence Length of Copolymers of Alkyl Methacrylates Probed by Pyrene Excimer Fluorescence

Kristijan Lulic and Jean Duhamel*

Institute for Polymer Research, Waterloo Institute for Nanotechnology, Department of Chemistry, University of Waterloo, ON N2L 3G1, Canada

INTRODUCTION

Engine oils perform many essential functions inside an engine beyond lubrication to maintain consistent performance.¹ These include cooling the engine by heat transfer,² cleaning deposits generated in the engine during use,³ and providing protection from corrosion that may occur from fuel combustion by-products.⁴ However, a base engine oil cannot accomplish these tasks on its own and requires the use of additives to enhance its properties. Engine oil additives have been the focus of concerted research efforts in order to improve the properties of oils, ensure that oils adhere to increasingly stricter emissions regulations, and limit their environmental impact.^{5, 6} One such issue is the decrease in oil viscosity that results from an increase in temperature as an engine begins operation.⁷ Depending on the latitude where a car is being operated, the engine temperature can be as low as $-40\text{ }^{\circ}\text{C}$ at start-up but as high as $110\text{ }^{\circ}\text{C}$ in some regions of the motor.⁸ Within this temperature range, the base oil experiences a significant decrease in viscosity, to the point, that it becomes too thin to perform as a lubricant, and consequently, protect engine components.⁷ In a similar sense, lower temperatures can pose their own set of challenges for engine oils. Below a specific temperature, referred to as the pour point, an oil loses its ability to flow because of crystallization of small amounts of wax left in commercial engine oils to increase their viscosity.⁹ Below its pour point, an engine oil can no longer flow throughout the engine to reduce component wear. In order to address these problems, a class of additives such as poly(alkyl methacrylate)s (PAMAs) are used as viscosity index improvers (VIIs) and pour-point depressants (PPDs).¹⁰⁻¹² VIIs are polymers that mitigate the significant drop in an oil's viscosity index. From the Guth-Einstein equation depicted in Equation 1, where ϕ_P is the fraction of the solution volume occupied by the polymer. An increase in temperature reduces the oil viscosity (η_o) if no polymer is added.¹³ However, with PAMA in the solution, ϕ_P increases with increasing temperature in a manner that offsets the decrease in the oil viscosity.

$$\eta = \eta_o \times B_1\phi_P + B_2\phi_P^2 + \dots \quad (1)$$

At low temperatures, PAMAs are relatively insoluble as a result of the polar ester functionality, adopting a contracted conformation minimizing contributions to overall viscosity. As temperature is increased, solubility improves, and the polymer coils expand.¹⁴ These properties rationalize the use of PAMAs as VIIs. PPDs on the other hand are used to extend the lower boundary of the temperature range over which oils flow.¹¹ The long side chains of PAMAs acting as PPDs co-crystallize with the growing wax crystals, with the polymer backbone hindering further growth of the wax crystals.¹⁵ Crystal growth is redirected into the formation of two-dimensional needle like structures as opposed to a three-dimensional mesh, delaying the onset of the oil's pour point.¹⁶ Although not explicitly described in the technical literature, PPDs are often PAMAs composed of alkyl side chains with different lengths. The longer side chains interact with wax and are required to disrupt wax network formation, while side chains of intermediate lengths impart

stability to the wax-polymer co-crystal. Shorter chains are incorporated to act as spacers that provide the polymer with enough flexibility to better fit into the crystal lattice structures.¹⁷ Although PPD efficacy is largely independent of molecular weight, there is a minimum backbone size in order to provide the requisite steric hindrance to inhibit wax crystal growth.

Polymer backbone flexibility is typically characterized by its persistence length, usually obtained through conformation plots generated by static light (SLS), small angle X-ray (SAXS), or neutron (SANS) scattering, intrinsic viscosity, or with a gel permeation chromatography (GPC) instrument equipped with a light scattering and/or viscosity detector. While the worth of these techniques at determining the persistence length is well-established, lesser known are the stringent requirements associated with their use. Scattering and intrinsic viscosity measurements require the preparation of a series of polymers with a narrow molecular weight distribution, which is not always achievable. GPC experiments require that the instrument be carefully calibrated and the absence of interactions between the polymer of interest and the column packing material.

In contrast to these challenges, the persistence length has been obtained through the analysis of fluorescence decays acquired with polymers randomly labeled with pyrene to take advantage of pyrene's ability to form an excimer. The efficiency of pyrene excimer formation (PEF) is proportional to the local pyrene concentration ($[Py]_{loc}$), and if pyrene is covalently attached to the polymer, the PEF efficiency is proportional to the local polymer density (ρ_{loc}). The extension of a polymer chain, corresponding to an increase in the persistence length, affects ρ_{loc} , $[Py]_{loc}$, and the PEF efficiency.¹⁸ The fluorescence blob model (FBM),¹⁹ which operates under the assumption that a pyrenyl label can only probe a certain volume around itself, referred to as a *blob*, while it remains excited, yields the number (N_{blob}) of structural units inside a *blob*. Since more flexible polymers yield larger N_{blob} values, N_{blob} is intrinsically related to the persistence length. The Duhamel Laboratory has applied PEF to a series of PAMA randomly labeled with pyrene, demonstrating that N_{blob} decreases, and thus the persistence length increases, with increasing length of the alkyl side chain in PAMAs.²⁰ With this in mind, a series of pyrene-labeled PAMAs were prepared by copolymerizing *n*-butyl and stearyl methacrylate with 1-pyrenebutyl methacrylate (Py-P(C₄MA-*co*-C₁₈MA)). Their fluorescence decays were acquired and fitted according to the FBM to yield N_{blob} values, that were compared against the previously determined Py-PAMA homopolymers. N_{blob} took a same value for the PAMA homo- and co-polymers with a structural unit sharing a same average molar mass, thus suggesting that these polymers would also share the same persistence length. Based on these results, the PEF-based methodology developed with Py-PAMA could become a useful tool for determining the persistence length of polymers.

EXPERIMENTAL

Chemicals: *n*-Butyl methacrylate, stearyl methacrylate, methacrylic anhydride, azobisisobutyronitrile (AIBN), 1-pyrenebutanol, dimethylaminopyridine (DMAP), toluene, methanol, and dichloromethane were purchased from Aldrich.

*Synthesis of the pyrene-labeled poly(*n*-butyl methacrylate-*co*-stearyl methacrylate):* Copolymers of butyl methacrylate (C₄MA), stearyl methacrylate (C₁₈MA), 1-pyrene butyl methacrylate (PyBuMA) (Py-P(C₄MA-*co*-C₁₈MA)) were prepared by free radical polymerization in toluene at 63 °C, using azobisisobutyronitrile (AIBN) as the initiator. The conversion of the monomer was kept below 20% to minimize composition drift. This was accomplished through the analysis of the

^1H NMR spectrum of the polymerization mixture acquired at different time intervals. Once a suitable conversion was reached, the reaction was terminated by exposure to air, and precipitated in chilled methanol, and centrifuged to remove any unreacted monomer. This procedure was repeated more than 5 times. Afterwards, the polymer was dried under vacuum for 12 hours to remove any residual solvent. The pyrene derivative used in these polymerizations was prepared by methacrylation of pyrene butanol by reacting 0.42 mL (2.8 mmol) of methacrylic anhydride with 0.50 g (1.8 mmol) of 1-pyrenebutanol in the presence of 0.0445 g (0.36 mmol) of dimethylaminopyridine in 50 mL of distilled dichloromethane. For each copolymer composition, the copolymerizations were conducted with a same C_4MA -to- C_{18}MA ratio and adjusting the amounts of 1-pyrenebutyl methacrylate to obtain 4-to-5 Py-P(C_4MA -*co*- C_{18}MA) samples with pyrene contents ranging from 0.5 to 6 mol%.

Chemical composition and molecular weight distribution of the copolymers: The pyrene content of the Py-P(C_4MA -*co*- C_{18}MA) samples was determined by measuring the absorbance of a Py-P(C_4MA -*co*- C_{18}MA) solution in THF of known mass concentration (m). The absorbance was determined at 344 nm with a Varian Cary 100 Bio UV-Visible spectrophotometer using a 1 cm pathlength cell. Applying Beer-Lambert's law with a molar extinction coefficient of 42,000 $\text{M}^{-1}\text{cm}^{-1}$ for 1-pyrenebutanol in THF yielded the pyrene concentration ($[\text{Py}]$). The molar fraction (x) of pyrene-labeled structural units in the copolymer was determined from the pyrene content ($\lambda_{\text{Py}} = [\text{Py}]/m$) with Equation 2, where y is the molar ratio of C_{18}MA to C_4MA ($y = x_{\text{C}_{18}\text{MA}}/x_{\text{C}_4\text{MA}}$). In Equation 2, $M_{\text{C}_{18}\text{MA}}$, $M_{\text{C}_4\text{MA}}$, and M_{Py} are the molar masses of stearyl methacrylate, n -butyl methacrylate, and 1-pyrenebutyl methacrylate equal to 338.6, 142.2, and 342.4 g/mol, respectively.

$$x = \frac{yM_{\text{C}_{18}\text{MA}} + M_{\text{C}_4\text{MA}}}{(1+y)/\lambda_{\text{Py}} + yM_{\text{C}_{18}\text{MA}} + M_{\text{C}_4\text{MA}} - (1+y)M_{\text{Py}}} \quad (2)$$

Between each set, three molar ratios y equal to 0.18, 1.0, and 3.0 were considered corresponding to 15, 50, and 70 mol% of C_{18}MA . The molar ratio was determined through the analysis of the ^1H NMR spectra acquired with all the Py-P(C_4MA -*co*- C_{18}MA) samples.

The molecular weight distribution of the copolymers was characterized by gel permeation chromatography (GPC) using a Viscotek GPC instrument with a 305 triple detection array that includes a differential refractive index (DRI), viscosity, and light scattering detectors.

Fluorescence analysis: The fluorescence measurements were conducted with the Py-P(C_4MA -*co*- C_{18}MA) samples dissolved in THF with a 0.1 OD corresponding to a pyrene concentration of 2.5 $\mu\text{mol/L}$ or a polymer concentration of about 5 mg/L. The solutions were degassed with nitrogen for 30 minutes to remove oxygen, a known fluorescence quencher. The fluorescence spectra were acquired from 350 to 600 nm after exciting the solution at 344 nm. For time-resolved fluorescence measurements, the excitation wavelength was set at 344 nm, with monomer and emission decays obtained at 379 and 510 nm, respectively. The FBM was then applied to analyze these fluorescence decays, fitting the monomer and excimer decays globally. Using several parameters from the FBM analysis, as well as the pyrene content (x in Equation 2), N_{blob} could be determined through Equation 3, where $\langle n \rangle$ is the average number of ground-state pyrenes per *blob* and f_{Mfree} is the molar fraction of free monomer detected in the monomer fluorescence decay.

$$\langle N_{\text{blob}} \rangle = \frac{1 - f_{\text{Mfree}}}{x} \times \langle n \rangle \quad (3)$$

RESULTS AND DISCUSSION

Three sets of Py-P(C₄MA-*co*-C₁₈MA) copolymers were prepared by free radical polymerization with contents of C₁₈MA monomer equal to 15, 50, and 70 mol% C₁₈MA. A set of polymers with the same C₁₈MA content was prepared with pyrene contents ranging from 2-6 mol%, and an additional polymer sample with a pyrene content smaller than 1 mol%, which was used as a model compound to determine the lifetime of the pyrene monomer. These polymers were characterized using absorption and time-resolved fluorescence to determine the pyrene contents and obtain the fluorescence decays, respectively. FBM analysis of the fluorescence decays yielded N_{blob} , which is plotted as a function of pyrene content in Figure 1A.

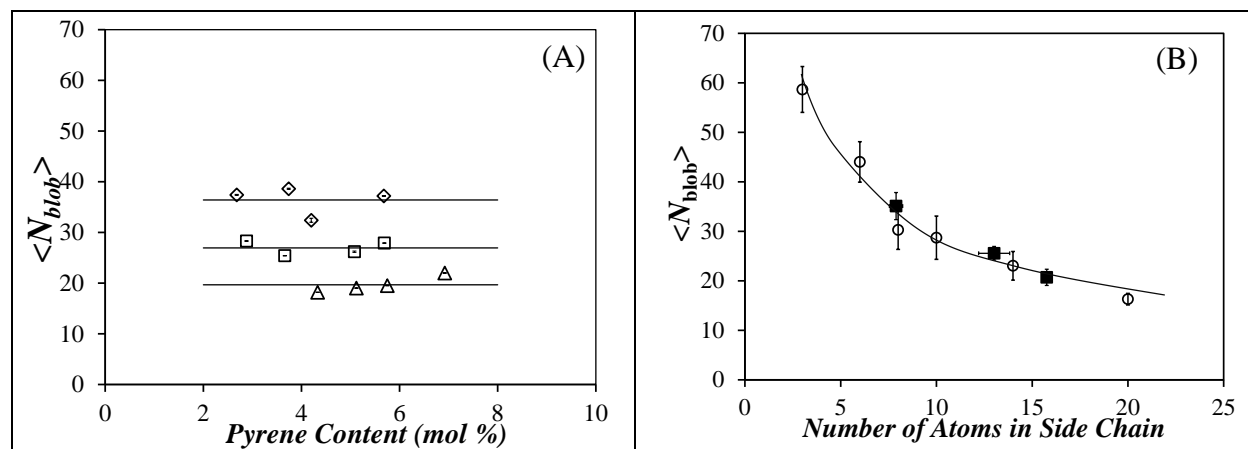


Figure 1. (A) Plot of N_{blob} as a function of pyrene content for Py-P(C₄MA-*co*-C₁₈MA) samples with varying C₁₈MA compositions (15 mol% C₁₈MA ($y = 0.18$; \diamond), 50 mol% C₁₈MA ($y = 1.0$; \square), and 70 mol% C₁₈MA ($y = 3.0$; \triangle)). (B) Plot of $\langle N_{\text{blob}} \rangle$ as a function of the number of carbon atoms in the side chain. (\circ) Py-PAMA homopolymers (PC₁MA, PC₄MA, PC₆MA, PC₈MA, PC₁₂MA, PC₁₈MA),²⁰ (\blacksquare) Py-P(C₄MA-*co*-C₁₈MA) copolymers (15% C₁₈MA, 50% C₁₈MA, and 70% C₁₈MA).

Within experimental error, N_{blob} remained constant with pyrene content. The N_{blob} values were averaged to yield $\langle N_{\text{blob}} \rangle$ which was plotted as a function of the average number ($\langle N_S \rangle$) of carbon atoms in the side chain of the Py-PAMA homopolymers previously studied,²⁰ for which $\langle N_S \rangle$ simply equals the side chain length, and the Py-P(C₄MA-*co*-C₁₈MA) samples, for which $\langle N_S \rangle$ was calculated according to Equation 4.

$$\langle N_S \rangle = 4 \times \frac{1}{1+y} + 18 \times \frac{y}{1+y} \quad (4)$$

For both the homopolymers and copolymers, N_{blob} was found to continually decrease with increasing alkyl side chain length from 59 (± 5) for Py-PC₁MA (poly(methyl methacrylate)) to 16 (± 1) for Py-PC₁₈MA (poly(stearyl methacrylate)). The decrease in N_{blob} is indicative of a decrease in backbone flexibility, with excited pyrenes probing a smaller volume within a polymer coil when the polymer becomes more extended due to the steric hindrance introduced by the longer alkyl side chains. Moreover, the N_{blob} values of 36 (± 3) for 15 mol% C₁₈MA, 27 (± 1) for 50 mol% C₁₈MA, and 20 (± 2) for 70 mol% C₁₈MA obtained for the Py-P(C₄MA-*co*-C₁₈MA) copolymers

matched those obtained for the homopolymers of equivalent side chain length, which suggests that the flexibility, and consequently the persistence length, of the polymethacrylate backbone depends on the average side chain length of the structural unit.

CONCLUSIONS

This study has established that N_{blob} for Py-P(C₄MA-co-C₁₈MA) copolymers matches the N_{blob} for Py-PAMAM homopolymers having a same equivalent side chain length. Since N_{blob} has been shown to depend directly on the persistence length of the PAMA sample, it suggests that the N_{blob} values obtained for the Py-P(C₄MA-co-C₁₈MA) copolymers can be used to predict their persistence length.

REFERENCES

- (1) Wong, V. W.; Tung, S. C. *Friction* **2016**, *4*, 1-28.
- (2) Hosny, A-Z. Z. *Energy Conversion and Management* **2004**, *45*, 2553-2569.
- (3) Mikkonen, S.; Niemi, A.; Niemi, M.; Niskala, J. *Journal of Fuels and Lubricants* **1989**, *98* (4), 1046-1056.
- (4) Ermolov, Énglin, A. B.; Vigant, G. T.; Zakharova, N. N. *Chemistry and Technology of Fuels and Oils* **1982**, *18* (3), 130-132.
- (5) Gligorijevic, R.; Jevtic, J. *Synth. Lubr* **2004**, *21*, 33-42.
- (6) Korcek, S.; Jensen, R. K.; Johnson, M. D.; Sorab, J. *Tribotest* **2001**, *7*, 187-201.
- (7) Covitch, M. J.; Trickett, K. J. *Adv. Chem. Eng. Sci.* **2015**, *5*, 134-151.
- (8) Roberts, A.; Brooks, R.; Shipway, P. *Energy Conversion and Management* **2014**, *82*, 327-350.
- (9) Ren, Y.; Chen, Z.; Du, H.; Fang, L.; Zhang, X. *Ind. Eng. Chem. Res* **2017**, *56*, 11161-11166.
- (10) Savoji, M. T.; Zhao, D.; Muisener, R. J.; Schimossek, K.; Schoeller, K.; Lodge, T. P.; Hillmyer, M. A. *Ind. Eng. Chem. Res* **2018**, *57*, 1840-1850.
- (11) Van Horne, W. L. *Ind. Eng. Chem.* **1949**, *41*, 952-959.
- (12) Van Horne, W. L. *Ind. Eng. Chem.* **1949**, *41*, 952-959.
- (13) Einstein, A. *Ann. d. Phys* **1906**, *19*, 289.
- (14) Barbadz, E. A.; Lamb, G. D. *Lubricant Additives: Chemistry and Application*. Rudnik, L. R., Ed.; CRC Press, Boca Raton: Florida, **2003**; pp 458-490.
- (15) Poornachary, S. K. ; Chia, V. D. ; Schreyer, M. K. ; Chow, P. ; Tan, R. B. H. *Crystal Growth & Design* **2022** *22*, 4031-4042.
- (16) Wang, C.; Chen, H.; Shi, H.; Ma, K.; Ma, Q.; Gong, J. *ACS Omega* **2022**, *7*, 11200-11207.
- (17) Pirouz, S.; Duhamel, J.; Jiang, S.; Duggal, . *Macromolecules* **2015**, *48*, 4620-4630.
- (18) Birks, J. B. *Photophysics of Aromatic Molecules*; Wiley: New York, **1970**; p 301.
- (19) Mathew, A.; Siu, H.; Duhamel, J. *Macromolecules* **1999**, *32*, 7100-7108.
- (20) Farhangi, S.; Weiss, H.; Duhamel, J. *Macromolecules* **2013**, *46*, 9738-9747.

Azin Adibi
Chemical Engineering
Waterloo

Development of biopolymer coating with high barrier performance based on enzymatic polysaccharide and natural rubber for paper-based packaging applications

Winner of the 2023 IPR Award for Academic Excellence in Polymer Science/Engineering

Development of biopolymer coating with high barrier performance based on enzymatic polysaccharide and natural rubber for paper-based packaging applications

Azin Adibi, Prof. Tizazu Mekonnen, Prof. Leonardo Simon

Institute for Polymer Research & Department of Chemical Engineering, University of Waterloo,
Waterloo, ON, Canada, N2L3G1

Abstract

Presently packaging market is mostly saturated with inexpensive and single-use petroleum-based polymers. Upon their first use, only a small fraction is recycled, which leads to the accumulation of these synthetic polymers in the landfills and environment and thus causes a threatening problem to the health of the environment [1]. Therefore, increased environmental concerns in combination with consumer demands for both greater quality and longer shelf life of packaging materials have led to the development of biodegradable, compostable, or recyclable paper-based packaging. The replacement of plastic with paper formats will result in a reduction in shelfstability and an increase in food waste from farm to table. It is, however, not possible to meet these sustainability objectives with typical paper-based formats due to their inadequate barrier performance[2]. Hence, surface coating with bio-based polymers is a well-established approach to confer the desired property to paper[3].

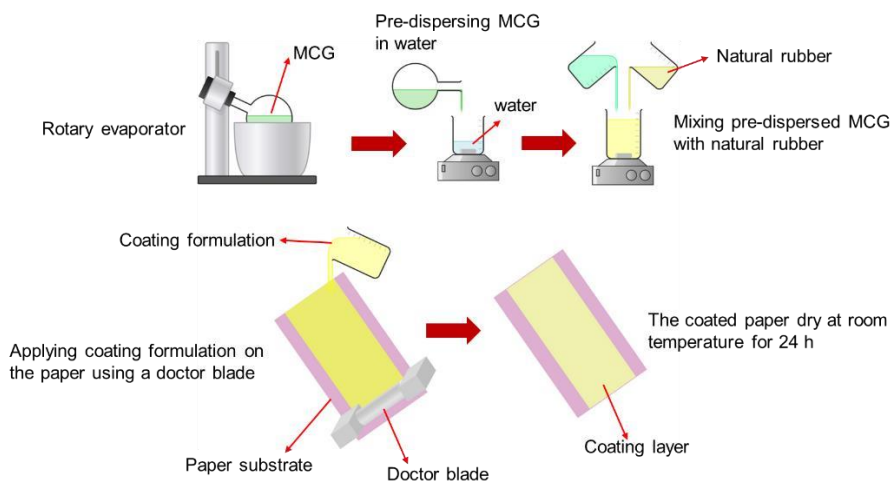
Natural rubber (NR) is an abundant renewable biopolymer extracted from the rubber tree (*Hevea brasiliensis*) in the form of a milky colloidal suspension [8]. NR is considered one of the most utilized elastomers and has extensive applications, particularly in coatings, adhesives, condoms, tires, gloves, and power transmission belts [9]. Properties, such as excellent film-

forming ability, high moisture barrier, recyclability, and flexibility could make NR an excellent alternative as coating for application in the packaging market. Nevertheless, at this point the utilization of NR in paper coatings is still limited [10]. This is because NR has certain limitations, such as poor mechanical, oil, and weather resistance that need to be addressed in order to achieve the essential requirements to fulfil the paper coating market needs. Employing polysaccharides as functional additives can compensate the drawbacks of NR to make it an appealing and environmentalfriendly material alternative to replace conventional polymers [11].

More recently, a novel approach was employed to produce engineered polysaccharide, alpha-1,3 glucan, by IFF (Former DuPont Nutrition and Biosciences). Alpha-1,3 glucan was obtained by enzymatic polymerization of glucose that is derived from sucrose. [12]. The alpha-1,3 glucan generated as such is a free-flowing powder, water-insoluble, linear, highly crystalline, with a high surface area [13]. Despite their high tendency to form agglomeration, alpha-1,3 glucan can be dispersed in water under shear to form a stable colloidal suspension. The enzymatic polymerization process allows control of morphologies, including spherical aggregates (wet cake), fibrils, and platelet particles referred to as microcrystalline glucan (MCG) [14]. In this work, platelet morphology MCG particles were used, with a goal of promoting oxygen and oil barrier properties owing to their morphology, high crystallinity, and high surface area.

Formulating MCG into NR may be able to efficiently address the flaws of NR in terms of barrier properties and be able to generate desirable sustainable paper coating formulations. The main objective of this work was to investigate the fabrication of a paper coating that provides adequate mechanical and barrier properties while maintaining environmental attributes (scheme 1). Also, it assesses the contribution of alpha-1,3 glucan in NR formulation in terms of barrier properties. In addition, the effect of light-crosslinking on the mechanical as well as barrier performance of formulated NR/MCG paper coatings is investigated. Analytical techniques, such

as tensile strength studies, rheology study, permeability testing such as water vapor and oxygen, Cobb test, and Kit test, were utilized to determine the properties of the formulated paper coatings.



Scheme 1. Schematic illustration of coating fabrication procedure

The mutual colloidal stability of the MCG in the NR phase assisted in the good dispersion stability and compatibility of the MCG in the NR coating formulation. Formulated NR/MCG coatings improved both the dry and wet strength as well as modulus compared to the uncoated paper substrate without compromising the flexibility of the coated paper. Also, incorporation of the MCGs in the NR formulations led to strong adhesion strength of coating films to the paper substrate due to the high affinity of the MCGs to the paper fibers – this suggests that only one coating will be required in this process and the need of additional adhesive layers is not needed. The series of coating under assessment indicated outstanding oil, grease and oxygen barrier properties with a good compromise with regard to water vapor and water barrier performance (Figure 1). By introducing a light crosslinking in the paper coating formulations further enhancements in barrier properties were achieved. Overall, the developed NR/MCG paper coating systems provides good mechanical properties and barrier properties which should meet the

requirements for many product categories in the food packaging market. This may enable the utilization of paper-based packaging formats to replace traditional thermoplastic resin-based solutions. The approach described here may also provide the option to offer a multitude of key barrier performance characteristics required for viable shelf-life performance of packaged goods from one single coating step on the base paper substrate compared with incumbent, multilayer complex flexible packaging solutions. This alone provides an existing opportunity to enable a sustainable paper-based packaging material alternative that is inherently based on renewable feedstocks, biodegradable within various food-contact environments and recycle enabled.

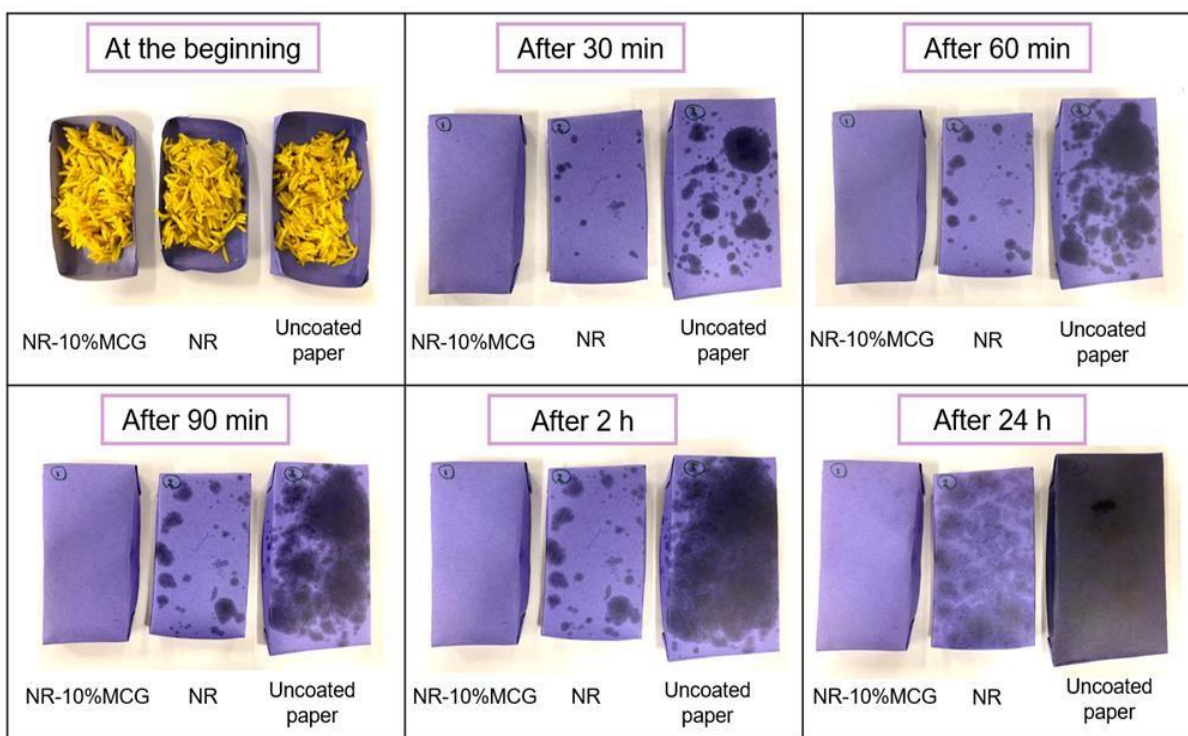


Figure 1. Oil barrier performance of paper coating samples.

References

- [1] B. E. Teixeira-Costa and C. T. Andrade, "Natural Polymers Used in Edible Food Packaging—History, Function and Application Trends as a Sustainable Alternative to Synthetic Plastic," *Polysaccharides 2022*, Vol. 3, Pages 32-58, vol. 3, no. 1, pp. 32–58, Dec. 2021, doi: 10.3390/POLYSACCHARIDES3010002.

- [2] C. Aulin, M. Gällstedt, and T. Lindström, “Oxygen and oil barrier properties of microfibrillated cellulose films and coatings,” *Cellulose*, vol. 17, no. 3, pp. 559–574, Jun. 2010, Accessed: Jun. 28, 2021. [Online]. Available: <https://link.springer.com/article/10.1007/s10570-009-9393-y>.
- [3] C. Andersson, “New ways to enhance the functionality of paperboard by surface treatment – a review,” *Packag. Technol. Sci.*, vol. 21, no. 6, pp. 339–373, Oct. 2008, doi: 10.1002/PTS.823.
- [4] E. Afra, S. Mohammadnejad, and A. Saraeyan, “Cellulose nanofibils as coating material and its effects on paper properties,” *Prog. Org. Coatings*, vol. 101, pp. 455–460, Dec. 2016.
- [5] S. Yook, H. H. Park, H. H. Park, S. Y. Lee, J. Kwon, and H. J. Youn, “Barrier coatings with various types of cellulose nanofibrils and their barrier properties,” *Cellulose*, vol. 27, no. 8, pp. 4509–4523, May 2020, doi: 10.1007/S10570-020-03061-5/FIGURES/10.
- [6] H. Li, Y. Qi, Y. Zhao, J. Chi, and S. Cheng, “Starch and its derivatives for paper coatings: A review,” *Prog. Org. Coatings*, vol. 135, pp. 213–227, Oct. 2019, doi: 10.1016/J.PORGCOAT.2019.05.015.
- [7] H. Chen *et al.*, “Application of Protein-Based Films and Coatings for Food Packaging: A Review,” *Polym. 2019, Vol. 11, Page 2039*, vol. 11, no. 12, p. 2039, Dec. 2019, doi: 10.3390/POLYM11122039.
- [8] J. Bras, M. L. Hassan, C. Bruzesse, E. A. Hassan, N. A. El-Wakil, and A. Dufresne, “Mechanical, barrier, and biodegradability properties of bagasse cellulose whiskers reinforced natural rubber nanocomposites,” *Ind. Crops Prod.*, vol. 32, no. 3, pp. 627–633, Nov. 2010.
- [9] R. Blanchard, E. O. Ogunsona, S. Hojabr, R. Berry, and T. H. Mekonnen, “Synergistic Crosslinking and Reinforcing Enhancement of Rubber Latex with Cellulose Nanocrystals for Glove Applications,” *ACS Appl. Polym. Mater.*, vol. 2, no. 2, pp. 887–898, 2020, doi: 10.1021/acsapm.9b01117.
- [10] P. Samyn, F. Driessen, and D. Stanssens, “Natural Rubber Composites for Paper Coating Applications,” in *Materials Proceedings 2020, Vol. 2, Page 29*, Aug. 2020, vol. 2, no. 1, p. 6832, doi: 10.3390/ciwc2020-06832.
- [11] S. Thakore, “Nanosized cellulose derivatives as green reinforcing agents at higher loadings in natural rubber,” *J. Appl. Polym. Sci.*, vol. 131, no. 16, p. 40632, Aug. 2014, doi: 10.1002/APP.40632.
- [12] D. Ganesarajan *et al.*, “Hybrid composites with engineered polysaccharides for automotive lightweight,” *Compos. Part C Open Access*, vol. 7, p. 100222, Mar. 2022, doi: 10.1016/J.JCOMC.2021.100222.
- [13] C. Lenges, N. Behabtu, J. Mok, I. Sendijarevic, and A. Sendijarevic, “Engineered polysaccharide alpha-1,3 glucan as isocyanate-reactive component in viscoelastic polyurethane foams,” *J. Appl. Polym. Sci.*, vol. 138, no. 10, p. 49979, Mar. 2021, doi: 10.1002/app.49979.
- [14] S. A. Kedzior *et al.*, “Elucidating the effect of enzymatic polymerized polysaccharide particle morphology on emulsion properties,” *Carbohydr. Polym.*, vol. 251, p. 117112, Jan. 2021, doi: 10.1016/j.carbpol.2020.117112.

Ryan Lloyd
Chemistry
Waterloo

Interactions Between DNA and Pyrene-Labeled Gemini Surfactant Probed by Fluorescence and Dynamic Light Scattering

Interactions Between DNA and Pyrene-Labeled Gemini Surfactant Probed by Fluorescence and Dynamic Light Scattering

Ryan Lloyd and Jean Duhamel

Institute for Polymer Research, Waterloo Institute for Nanotechnology, Department of Chemistry, University of Waterloo, ON, N2L 3G1, Canada

INTRODUCTION

Gemini surfactants (GS) have attracted recent research interest due to a variety of potential applications, such as their usage for improving oil recovery and the development of vectors for drug loading and release.¹ One important research application however is their use as potential gene transfection agents for gene delivery.^{2,3} In this context, a significant challenge in the field of gene therapy is the successful delivery of therapeutic genes to the desired cell.³ Successful delivery of the genetic cargo to the desired cell requires an effective delivery vector, that can efficiently interact with the cell membrane.⁴ These desirable membrane interactions were made possible by modifying the chemical structure of cationic gemini surfactants (CGS). Past studies have shown that CGS can form high and low order structures to efficiently interact with endosomal and model membranes.⁴ The versatility of gemini surfactants in generating a variety of aggregate types is due to the modularity of their chemical structure composed of building blocks (spacer, head groups, hydrophobe), that can be easily modified. The length and structure of the alkyl tails, as well as the length and nature of the alkyl spacer can all be optimized to maximize transfection efficiency.^{2,3} Additionally, surfactants with a lower CMC were found to be most efficient at compacting DNA. This means that the greater the tendency for a surfactant to self-aggregate at lower concentrations, the stronger the surfactant/DNA complexation.¹ Therefore, delivery vectors for gene therapy can be improved by developing a better chemical understanding of the interactions between DNA and surfactants. In this context, molecular level information about the lipoplexes formed between DNA and cationic surfactants can be obtained through the analysis of the fluorescence spectra and decays acquired with a small amount of the pyrene-labeled cationic gemini surfactant PyO-3-12 embedded in a lipoplex (Figure 1). These experiments take advantage of the ability of the dye pyrene to form an excimer upon encounter between an excited and a ground-state pyrene and the fact that the process of pyrene excimer formation (PEF) depends on the local pyrene concentration in the lipoplexes.⁵

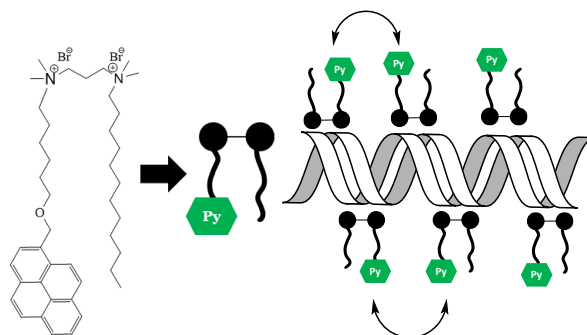


Figure 1. Molecular structure of PyO-3-12 (left). Schematic representation of the electrostatic interactions between PyO-3-12 and DNA leading to intermolecular pyrene excimer fluorescence (right).

When PEF occurs within and/or among pyrene-labeled macromolecules, a pyrenyl label is found in one of three states.⁶ Upon absorption of a photon, an excited pyrenyl label can be either isolated (Py_{free}^*) in a pyrene-poor domain of the macromolecule, where it emits with the lifetime τ_M of the pyrene monomer, or it can form an excimer either upon diffusive encounter with a ground-state pyrene (Py_{diff}^*) or via direct excitation of a pyrene aggregate (Py_{agg}^*).⁶

The fluorophore pyrene is widely used to characterize macromolecules due to its long lifetime, high quantum yield, and especially for its ability to form excimer.⁶ Past research has used a pyrene-labeled surfactant to study its interactions with DNA.⁷ While these earlier studies used an alkyl spacer to link pyrene to the surfactant, introduction of a heteroatom such as oxygen in the position beta-to-pyrene, as was done with the surfactant PyO-3-12 (see Figure 1), enables the pyrenyl label to sense the polarity of its local environment. This is achieved by monitoring its I_1/I_3 ratio, which represents the ratio of the fluorescence intensity of the first peak (I_1) over that of the third peak (I_3) in the steady-state fluorescence spectrum of the pyrene monomer.¹⁰ The transition corresponding to the first fluorescence band (I_1), which is also the 0-0 transition for pyrene, is very weak in apolar solvents, to the point that it is described as symmetry forbidden in numerous publications, but is significantly stronger in more polar solvents, which explains the sensitivity of the I_1/I_3 ratio to solvent polarity, taking a value of 0.58 in hexane or 1.87 in water.⁵

Studies utilizing methods based on pyrene excimer fluorescence typically employ two major techniques. The first technique is steady-state fluorescence, which involves the acquisition of an emission spectrum ranging from 350 to 600 nm. The areas under the fluorescence spectrum corresponding to the regions of emission for the pyrene monomer (I_M) and pyrene excimer (I_E) can be used to calculate the I_E/I_M ratio, which can be related to several parameters pertaining to the system under study according to Equation 1.⁶

$$\langle k \rangle = k_{diff} \times [Py]_{loc} \propto \frac{I_E}{I_M} \quad (1)$$

The I_E/I_M ratio is proportional to the average rate constant of PEF, which is equal to the product of the bimolecular rate constant k_{diff} for PEF times the local concentration $[Py]_{loc}$ of ground-state pyrene. k_{diff} in Equation 1 reflects the internal dynamics of a system such as those experienced by the surfactant PyO-3-12 bound to DNA as it forms excimer (see Figure 1). Due to the permanent positive charges of PyO-3-12, addition of DNA to a dilute PyO-3-12 aqueous solution results in the association of PyO-3-12 with DNA. In the process, PyO-3-12 is transferred from the polar aqueous solution to the hydrophobic environment of the PyO-3-12 aggregates bound to DNA, where it is concentrated and forms excimer.⁷ Consequently, the dilute PyO-3-12 aqueous solution yields a low I_E/I_M ratio since $[Py]_{loc}$ is low in Equation 1 and a large I_1/I_3 ratio characteristic of pyrene in polar water. Upon complexing DNA, the dilute PyO-3-12 with DNA yields a large I_E/I_M ratio since $[Py]_{loc}$ is large inside the PyO-3-12 aggregates bound to DNA and I_1/I_3 takes a lower value characteristic of the more hydrophobic environment of the PyO-3-12 aggregates. In summary, the fluorescence of pyrene represents a powerful analytical tool to study colloidal systems in water, whose application remains rudimentary in the literature. In particular, it is one of the very few techniques that allows investigators to study the behavior of polymers and surfactants at the molecular level in solution.

To complement the fluorescence techniques that probe soft matter at the molecular level, both dynamic (DLS) and static (SLS) light scattering can be utilized to study at the macroscopic level colloidal aggregates generated through complexation between polymers and surfactants in solution. In the present study, DLS is applied to characterize the size and zeta potential of the PyO-3-12/DNA aggregates. Combining the study of the PyO-3-12/DNA complexes at the molecular

level by fluorescence and at the macroscopic level by DLS provides a complete characterization of these aggregates.

EXPERIMENTAL

Chemicals: Deoxyribonucleic acid from calf thymus (CT-DNA) was purchased from Sigma-Aldrich. Doubly distilled deionized water from Millipore Milli-RO 10 Plus and Milli-Q UF Plus (Bedford, MA) was used to prepare all aqueous solutions.

Synthesis of PyO-3-12: It was carried out according to the reaction scheme shown in Figure 2.

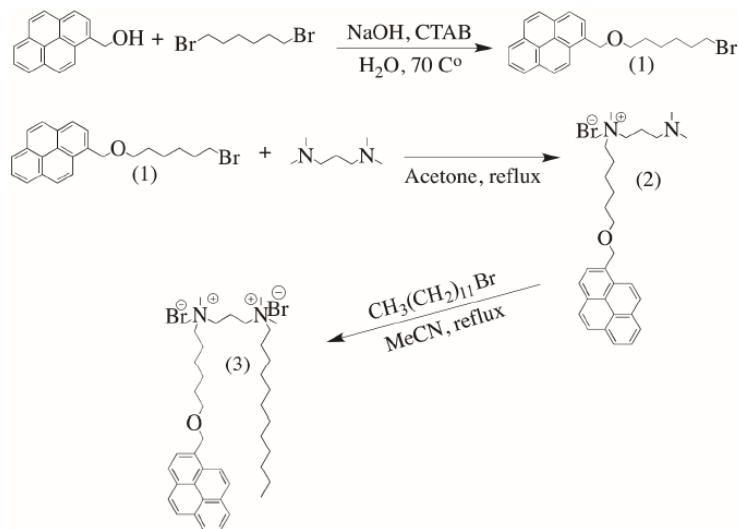


Figure 2. Reaction scheme for the synthesis of PyO-3-12.

Solution preparation: A PyO-3-12 concentration of 32 mM, below the CMC of PyO-3-12 equal to 0.38 mM, was used in all fluorescence experiments. The $(-/+)$ ratio represented the concentration ratio of DNA base pairs over PyO-3-12, keeping in mind that one DNA base pair and one PyO-3-12 molecule have two negative and two positive charges, respectively. The $(-/+)$ ratio was used to express the relative concentration of DNA with respect to the PyO-3-12 concentration. A solution of the desired $(-/+)$ ratio was obtained by preparing two solutions, one with double the desired concentration of CT-DNA and the other with double the desired concentration of PyO-3-12. Mixing 2 mL of each solution produced a mixture of CT-DNA and PyO-3-12 of the desired $(-/+)$ ratio. The solutions were left for at least one hour to reach equilibrium before being analyzed by dynamic light scattering, steady-state fluorescence, and time-resolved fluorescence.

Dynamic light scattering: The Particle size distribution (PSD) and ζ potential was determined on a Malvern Zetasizer Nano ZS 90 with a He-Ne laser (633 nm) at 90° at 25°C . The data were analyzed with the Malvern Dispersion Technology Software 4.20. The ζ -potential was determined by measuring the electrophoretic mobility using the Smoluchowski approximation. Measurements were repeated 3 times to obtain the number average size and the ζ -potential for each sample.

RESULTS AND DISCUSSION

The I_E/I_M and I_1/I_3 ratios retrieved from the analysis of the fluorescence spectra were expressed as a function of the $(-/+)$ ratio and they are shown along with the fluorescence spectra acquired at DNA concentrations below and above the equicharge point in Figure 3. The fluorescence spectra of PyO-3-12 show little excimer being formed at low $(-/+)$ ratios but a rapid increase in PEF is observed as the $(-/+)$ ratio approaches unity. Past the equicharge point, the excimer signal remained high, indicating strong PEF, although a small decrease was observed for increasing $(-/+)$ ratios. These trends were summarized in Figure 3C, where the I_E/I_M ratio was plotted as a function

of the (-/+) ratio. The significant increase in I_E/I_M observed at the equicharge point confirms the binding of PyO-3-12 to CT-DNA, since PyO-3-12 at a low concentration of 32 μM cannot micellize in solution and cannot form excimer unless it formed aggregates with CT-DNA.

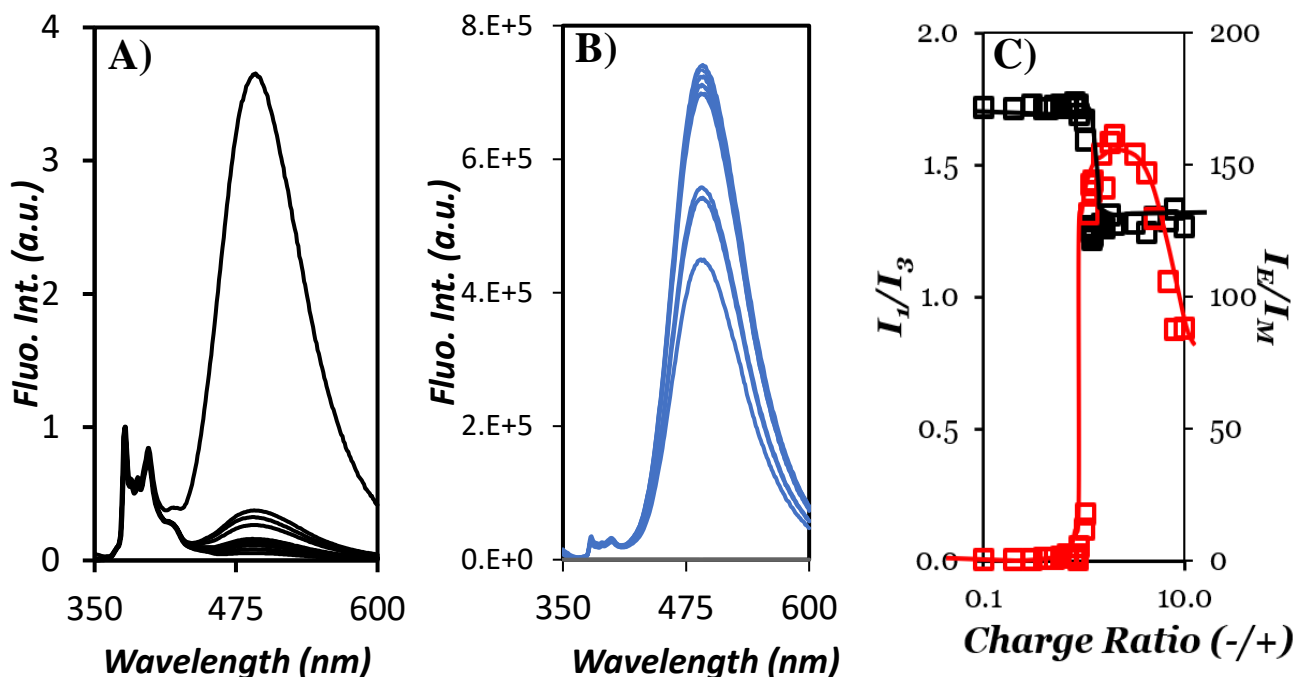


Figure 3. Normalized SSF spectra for (-/+) ratios ranging from A) 0 to 1.0 and B) 1.1 to 10, and C) plot of I_E/I_M and I_1/I_3 as a function of the (-/+) ratio. [PyO-3-12] = 32 μM , λ_{ex} = 344 nm.

PyO-3-12 is sensitive to the polarity of its local environment through the I_1/I_3 ratio. I_1/I_3 was plotted in Figure 3C as a function of the (-/+) ratio. For (-/+) ratios lower than the equicharge point, I_1/I_3 remained constant and equal to 1.72 (± 0.01), close to the I_1/I_3 ratio reported to equal 1.73 for PyO-3-12 in water. However, the I_1/I_3 ratio showed a significant and sudden drop at the equicharge point, above which it equaled 1.27 (± 0.02) for (-/+) ratios larger than 1.3.⁸ The I_1/I_3 ratio found for the PyO-3-12/CT-DNA complexes suggests that PyO-3-12 experiences a less polar environment than that experienced for PyO-3-12 in water, confirming that PyO-3-12 self-assembled into PyO-3-12 aggregates upon binding onto CT-DNA.⁸

A similar trend is observed for the zeta potential of solutions containing 32 μM PyO-3-12 and increasing CT-DNA concentration. Upon reaching the equicharge point, a charge inversion occurs. While the zeta potential remains positive and equal to 3.5 (± 1.3) mV below the equicharge point, the zeta potential turns negative and equals -46 (± 7) mV for (-/+) ratios above unity. The charge inversion was correlated to an increase in the number average hydrodynamic diameter (D_h) of the PyO-3-12/ct-DNA aggregates. This increase in D_h at the equicharge point is reasonable since all charges are neutralized, which reduces the solubility of the species in solution leading to their aggregation into larger objects. As the CT-DNA concentration increases past the equicharge point, the PyO-3-12 molecules distribute themselves across a larger number of DNA strands and the PyO-3-12/CT-DNA aggregates are negatively charged and better stabilized by electrostatic repulsion, leading to a reduction in D_h . As the CT-DNA concentration increases much further from

the equicharge point, the positively charged PyO-3-12 aggregates act as crosslinking points bridging different negatively charged CT-DNA strands resulting in the formation of a large CT-DNA network with a very large D_h .

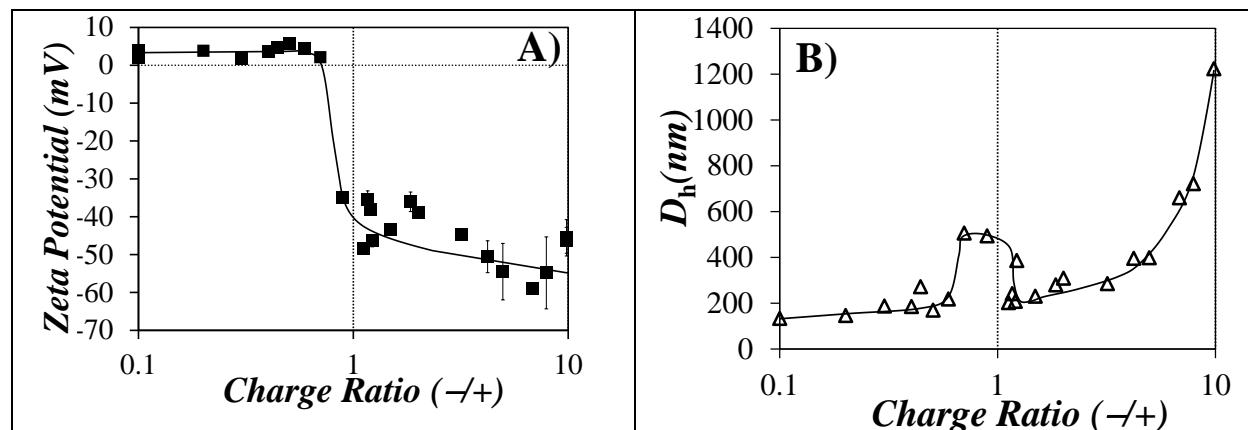


Figure 4. Plot of A) the zeta potential and B) the number average hydrodynamic diameter (D_h) for a 32 μ M PyO-3-12 aqueous solution as a function of the CT-DNA concentration.

CONCLUSIONS

In summary, the study of the electrostatic interactions between cationic surfactants (CS) and DNA and the structural arrangement of the CS in CS/DNA complexes represents an important field of research. Since fluorescence reports on the complexation of PyO-3-12 with CT-DNA, it must be able to characterize the spatial arrangement of the CS in CS/DNA aggregates. In turn, this feature might help predict gene transfection efficiency, since it is related to the structure of lipoplexes. It will also provide a greater understanding, possibly enabling the prediction, of the structures generated through the complexation between CS and DNA. DLS measurements in Figure 4 confirmed the strong electrostatic interactions between PyO-3-12 and CT-DNA, that were identified by fluorescence in Figure 3. This greater understanding of CS/DNA lipoplexes could be applied to prepare more efficient gene transfection agents, thus pushing the current limits of drug delivery and gene therapy.

REFERENCES

1. Wettig, S.; Verrall, R.; Foldvari, M. Gemini Surfactants: A New Family of Building Blocks for Non-Viral Gene Delivery Systems. *Curr Gene Therapy* **2008**, *8*, 9–23.
2. Kirby, A.J.; Camilleri, P. Gemini surfactants: New synthetic vectors for gene transfection. *Angew. Chem. Int. Ed.* **2003**, *42*, 1448–1457.
3. Ren, S.; Wang, M.; Wang, C.; Wang, Y.; Sun, C.; Zheng, Z.; Cui, H.; Zhao, X. Application of Non-Viral Vectors in Drug Delivery and Gene Therapy. *Polymers* **2021**, *13*, 3307–3316.
4. Bell, P. C.; Bergsma, M.; Dolbnya, I. P.; Bras, W.; Stuart, M. C. A.; Rowan, A. E.; Feiters M. C.; Engberts J. B. F. N. Transfection Mediated by Gemini Surfactants: Engineered Escape from the Endosomal Compartment. *J. Am. Chem. Soc.* **2003**, *125*, 1551–1558.
5. Ba Salem, A. Probing the Interactions between Pyrene-labelled Gemini Surfactants and DNA by Fluorescence. PhD thesis at UW, 2022
6. Duhamel, J. Global Analysis of Fluorescence Decays to Probe the Internal Dynamics of Fluorescently Labeled Macromolecules. *Langmuir* **2014**, *30*, 2307–2324.
7. Ba-Salem, A. O.; Duhamel, J. Synthesis and Characterization of a Pyrene-Labeled Gemini Surfactant Sensitive to the Polarity of Its Environment. *Langmuir* **2021**, *37*, 13824–13837.
8. Ba-Salem, A.; Gong, R.; Duhamel, J. Characterization of the Interactions between a Cationic Pyrene-Labeled Gemini Surfactant, and the Anionic Surfactant Sodium Dodecyl Sulfate. *Langmuir* **2022**, *38*, 7484–7495.

Franklin Frasca
Chemistry
Waterloo

Conformation of Pyrene-Labelled Polyamines
Established Through Their Molecular
Parameterization

Conformation of Pyrene-Labeled Polyamines Established Through their Molecular Parameterization

Franklin Frasca and Jean Duhamel

INTRODUCTION

The ability of pyrene to fluoresce differently whether it exists either as a lone monomer or an excited dimer, also known as an excimer formed upon the encounter between a ground-state and an excited pyrene, provides a powerful tool for obtaining information about the dynamics and conformation of macromolecules of any size in solution. Pyrene excimer formation (PEF) allows for the characterization of many complex pyrene-labeled macromolecules (PyLMs) in solution which would be difficult to characterize by any other common techniques based on scattering, viscosity, or NMR experiments. Due to the high molar extinction coefficient and fluorescence quantum yield of pyrene, PEF also enables the study of PyLMs under extremely dilute conditions ($\sim 1 - 10$ mg/L) which provides an unperturbed view of the PyLM of interest. This is in direct contrast to most other techniques which often require concentrations ($\sim 1 - 10$ g/L) that are so high that the polymers are likely undergoing intermolecular interactions, further complicating the resolution of the internal dynamics and conformation of single macromolecules. While many experiments have been conducted to get a qualitative measure of the PEF efficiency, for example using the I_E/I_M ratio to determine the relative amounts of excimer and monomer fluorescence, respectively, the quantitative analysis of PEF remains difficult and as a result is much more rarely used to glean information on macromolecular dynamics and conformation.

In earlier works, PEF was used to determine the rate of end-to-end cyclization (k_{cy}) of monodisperse linear chains with a pyrene appended to each end by using time-resolved (TRF) and steady-state (SSF) fluorescence.¹⁻³ These studies took advantage of the theoretical work by Wilemski and Fixman,^{4,5} who had found that the slowest internal relaxation time of a polymer was the rate constant k_{cy} of end-to-end cyclization, which was proportional to the rate constant for PEF determined through analysis of the fluorescence decays of the pyrene end-labeled polymer. While useful, this study highlighted the requirement for monodisperse chains for the accurate determination of k_{cy} , which provided the internal relaxation time of a polymer. Furthermore, the limitation of having only two pyrenes per molecule restricted the determination of k_{cy} to chains that were sufficiently short to enable PEF between the two terminal pyrenyl labels. Following this preliminary work, numerous other studies and models were developed in an attempt to better quantify polymer dynamics and conformation using PEF, namely the Model Free Analysis (MFA) which makes no assumptions about the nature of excimer formation to determine the average rate constant of PEF ($\langle k \rangle$), and the Fluorescence Blob Model (FBM) which views a polymer which has been randomly labeled with pyrene as a series of blobs in which the pyrenes can only form excimer within a blob to yield information on polymer backbone structure and flexibility.

Because PEF is a bimolecular process, the rate of PEF depends on the local pyrene concentration ($[Py]_{loc}$) of a pyrene-labeled molecule in solution given by Equation 1. In Equation 1, $\langle L_{Py}^2 \rangle^{1/2}$ represents the average end-to-end distance between two pyrenyl labels on the PyLM defining a spherical volume equal to $4p \times (\langle L_{Py}^2 \rangle^{1/2} / 2)^3 / 3$ capable of accommodating a set number of ground-state pyrenes. The general scheme of PEF and the associated SSF spectrum of a pyrene-labeled small molecule (PyLsM) are shown in Figure 1.

$$[Py]_{loc} = \frac{\# \text{ of G.S.Pyrenes}}{\frac{4}{3}\pi \left(\frac{\langle L_{Py}^2 \rangle^{1/2}}{2} \right)^3} \quad (1)$$

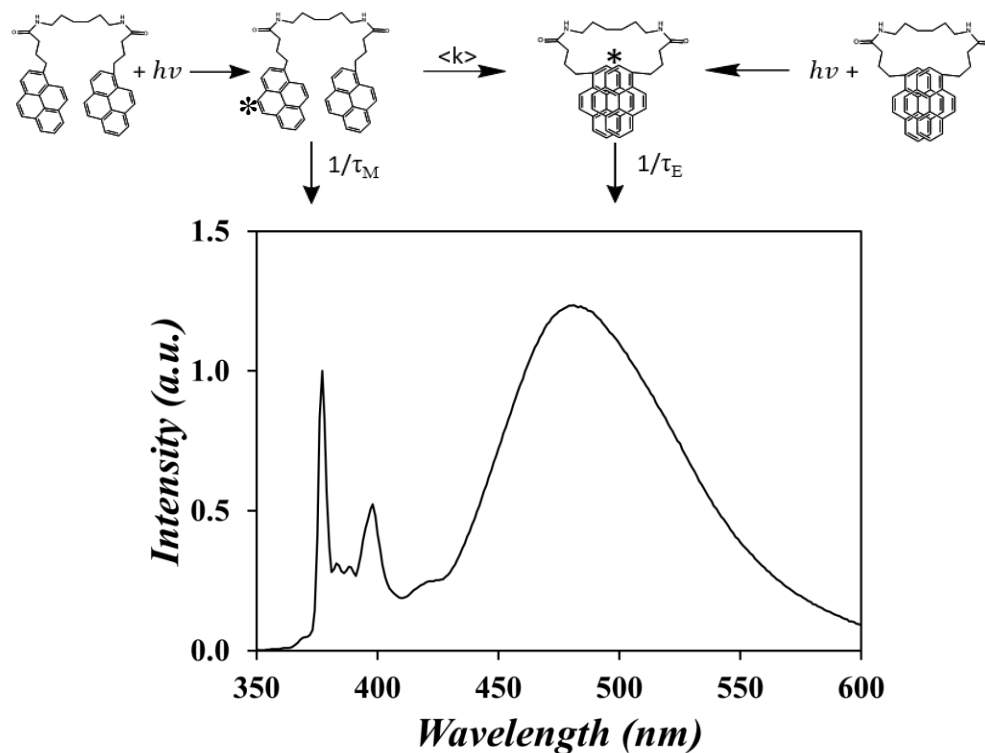


Figure 1. Top: The general scheme of PEF. Bottom: The steady-state fluorescence spectrum of hexamethylene *bis*(1-pyrenebutyramide) (Py₂-HMDA), normalized to the monomer peak at 377 nm; $\lambda_{\text{ex}} = 344$ nm, $[\text{Py}] = 2.5 \times 10^{-6}$ M in THF.

Analysis of SSF spectra can provide qualitative information on PEF via integration of the excimer and monomer emissions between 500 – 530 and 372 – 378 nm, respectively, to yield the I_E/I_M ratio and gauge the relative amounts of excimer and monomer fluorescence of the PyLM of interest in solution. While useful for many studies, the SSF spectra are prone to suffer from several artifacts due to solvent effects, aggregation of the pyrenyl labels (right pathway for PEF in the reaction scheme shown in Figure 1), and/or the presence residual unreacted pyrene derivative used in the preparation of the PyLM which can distort the spectra and greatly complicate the use of the I_E/I_M ratio. On the other hand, MFA of the monomer and excimer decays obtained through TRF measurements can yield both the molar fractions of different pyrene species contributing to PEF and $\langle k \rangle$, the average rate constant for PEF by diffusion (left pathway for PEF in the reaction scheme in Figure 1). The MFA of the TRF decays also yields the molar fractions f_{diff} , f_{agg} , and f_{free} representing the pyrene forming excimer diffusively, through aggregation, or not forming excimer and fluorescing as monomer, respectively. The molar fractions can provide information on both the extent of free pyrene impurities in solution and through which pathway, either diffusive or aggregation, the excimer is being formed through. The number average lifetime ($\langle t \rangle$) is obtained through the MFA and is used to determine $\langle k \rangle$ as seen in Equation 2. Both $\langle k \rangle$ and the I_E/I_M ratio have been shown in previous work to be proportional to $[\text{Py}]_{\text{loc}}$ based on Equation 3. ⁷ k_{diff} in Equation 3 is the bimolecular rate constant for PEF by diffusion. Since $[\text{Py}]_{\text{loc}}$ is related to the conformation of the macromolecule through L_{Py} , so is $\langle k \rangle$ according to Equation 3.

$$\langle k \rangle = \frac{1}{\langle \tau \rangle} - \frac{1}{\tau_M} \quad (2)$$

$$\frac{I_E}{I_M} \propto k_{diff} \times [Py]_{loc} = \langle k \rangle \quad (3)$$

The linear relationship between $\langle k \rangle$, the I_E/I_M ratio, and $[Py]_{loc}$ has thus far only been demonstrated quantitatively for a series of pyrene-labeled dendrimers. ^{Error! Bookmark not defined.} This work serves to extend the validity of this relationship to both PyLMs and PyLsM to further validate this PEF-based methodology of extracting information on the internal dynamics and conformation of pyrene-labeled molecules in dilute solution.

EXPERIMENTAL

A series of pyrene-labeled polyamines (Py-PAs) whose structures are shown in Figure 2, were synthesized yielding both doubly end-labeled linear chains and branched architectures having more than two pyrenyl moieties. Dilute solutions of each Py-PA were prepared in THF, DMF, and DMSO, a set of common organic solvents which solubilize a wide range of both synthetic and bio-based polymers. Their SSF spectra were acquired to yield their I_E/I_M ratios, and MFA of the monomer and excimer TRF decays yielded their $\langle k \rangle$ values, respectively. Each Py-PA was diluted to $[Py] = 2.5 \times 10^{-6}$ M before acquisition of the SSF spectra and monomer and excimer TRF for analysis with the MFA.

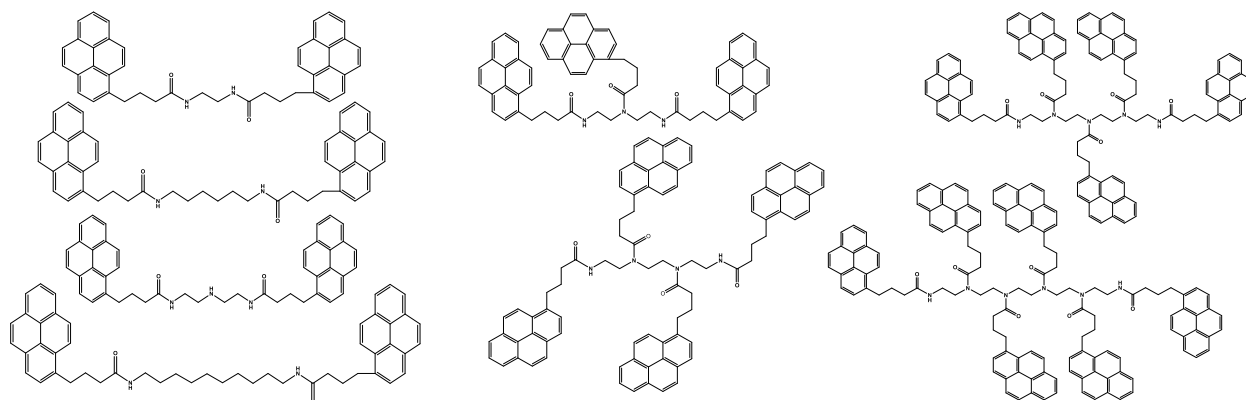


Figure 2. Chemical structures of the Py-PAs prepared for this study.

RESULTS & DISCUSSION

Integration of the SSF spectra and MFA of the TRF decays yielded the I_E/I_M ratio and $\langle k \rangle$, respectively, for each Py-PA in THF, DMF, and DMSO. $[Py]_{loc}$ was calculated for each Py-PA according to Equation 1 to generate plots of $\langle k \rangle$ -vs- $[Py]_{loc}$ in each solvent studied, which are shown in Figure 3.

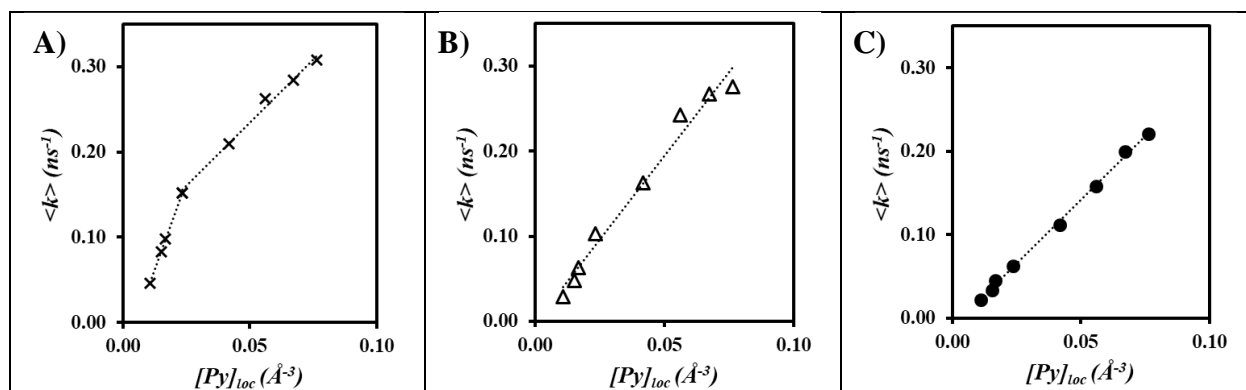


Figure 3. Plots of $\langle k \rangle$ -vs- $[Py]_{loc}$ obtained from the MFA of the monomer and excimer fluorescence decays for each Py-PA in A) THF, B) DMF, and C) DMSO; $[Py] = 2.5 \times 10^{-6}$ M.

$\langle k \rangle$ is seen to have a linear response w.r.t $[Py]_{loc}$ in both DMF and DMSO, supporting the validity of Equation 1 for determination of $[Py]_{loc}$ and in turn the internal density of PyLMs in solution, now for a series of small molecules. The greater slope and $\langle k \rangle$ values in Figure 3B compared to Figure 3C reflect the higher viscosity of DMSO compared to DMF which slows the rate of excimer formation by diffusion.

A deviation from linearity is seen for the Py-PAs in THF, which could be due to the very low viscosity of THF ($\eta = 0.46$ mPa.s @ 25 °C) compared to DMF and DMSO ($\eta = 0.79$ and 2.0 mPa.s @ 25 °C, respectively). The linear trend for the lower $\langle k \rangle$ values obtained for the end-labeled polyamines deviated from the linear trend for the higher $\langle k \rangle$ values obtained for the branched Py-PAs bearing 3 or more pyrenes. The branched Py-PAs were also the only compounds containing hindered tertiary amides in addition to the less restricted secondary amides at the ends of each Py-PA. The high-viscosity solvents could be limiting the dynamics of the Py-PAs to be only viscosity-dependant, whereas the low viscosity THF could be resolving the difference in backbone dynamics between the branched and linear Py-PAs now that they were not sufficiently slowed by the solvent.

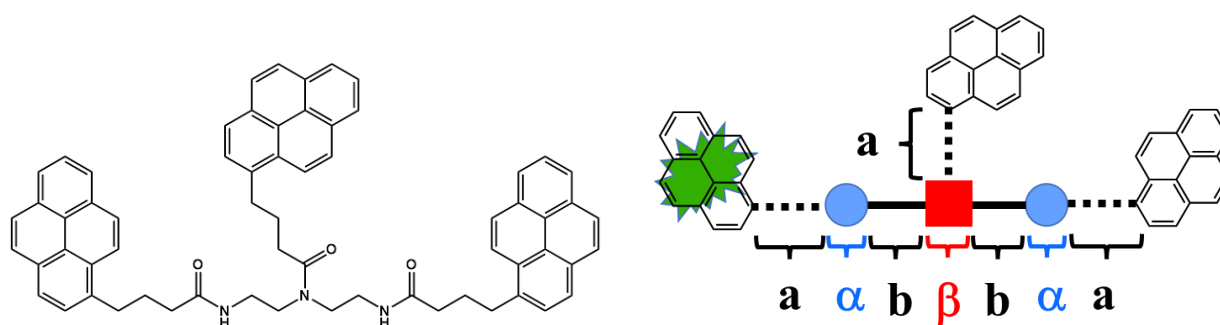


Figure 4. Left: The structure of the Py₃-DETA molecule. Right: The Py₃-DETA molecule as viewed during our molecular parameterization.

To further investigate this, we applied a method we termed *molecular parameterization* to assign different bond lengths to each segment of the Py-PAs. Since a reduced flexibility (reduction in k_{diff} in Equation 1) around the tertiary amides would be synonymous with an increase in bond length spanned by the amide (increase in $\langle L_{Py}^2 \rangle$ and reduction in $[Py]_{loc}$ in Equation 1) according

to $\langle k \rangle$ obtained from the MFA, this *molecular parametrization* assigns a bond length (b in Figure 4) to the tertiary amides in the branched polyamines, that can be adjusted compared to the other segment lengths (a , b , and a in Figure 4) for the calculation of $\langle L_{Py}^2 \rangle^{1/2}$. In turn, b can be optimized to linearize the plot of $\langle k \rangle$ -vs- $[Py]_{loc}$, where $[Py]_{loc}$ is obtained with Equation 1 from $\langle L_{Py}^2 \rangle^{1/2}$, and determine the extent of the difference in dynamics of the secondary and tertiary amides with respect to the methylene groups. $\langle L_{Py}^2 \rangle$ is calculated with Equation 4, wherein the # of walks is the number of pathways from one pyrene to another, and the # of encounters of i^{th} segment is the frequency with which each segment is encountered along all walks. l_i represents the squared average end-to-end distance of a given walk. The average # of encounters of each segment are used to calculate $\langle L_{Py}^2 \rangle^{1/2}$ for the Py-PAs, which in-turn yields the calculated values of the local pyrene concentration ($[Py]_{loc}^{cal.}$).

$$\langle L_{Py}^2 \rangle = \sum_{i=1}^n l_i^2 \times \frac{\# \text{ of encounters of } i^{th} \text{ segment}}{\# \text{ of walks}} \quad (4)$$

With this approach, the values of 4, 1, and 2 are assigned to parameters a , a , and b in Figure 4, corresponding to the number of atoms in each segment. The value of b is then optimized to yield the straightest line in a plot of $\langle k \rangle^{exp}$ -vs- $[Py]_{loc}^{cal.}$. This process yielded b values of 3.82, 2.57, and 0.88 in THF, DMF, and DMSO, respectively. This result supports our hypothesis that the tertiary amides have a much greater impact on the molecular dynamics in the less viscous THF, where the b value was the highest, than in more viscous DMF and DMSO. The plots of $\langle k \rangle^{exp}$ -vs- $[Py]_{loc}$ and $[Py]_{loc}^{cal.}$ -vs- $[Py]_{loc}$ in Figure 5 show that the optimized $[Py]_{loc}^{cal.}$ values yield $\langle k \rangle$ -vs- $[Py]_{loc}$ trends that mimic the experimental ones, further supporting that this molecular parameterization provides a more accurate measure of $[Py]_{loc}$ and in-turn a gauge of the effect that tertiary amides have on the internal dynamics of the Py-PAs.

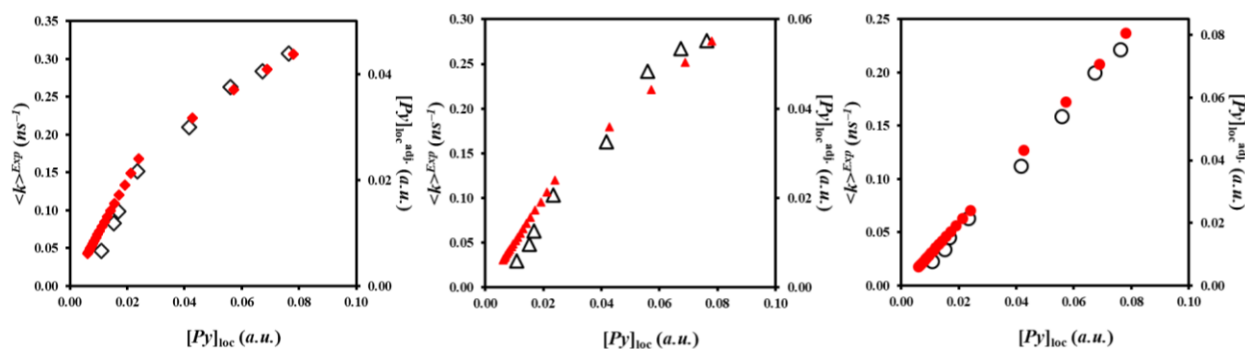


Figure 5. Plots of (black) $\langle k \rangle^{exp}$ -vs- $[Py]_{loc}$ and (red) $[Py]_{loc}^{cal.}$ -vs- $[Py]_{loc}$ in A) THF, B) DMF, and C) DMSO.

CONCLUSIONS

A series of Py-PAs were synthesized and their SSF spectra and TRF decays were acquired and analysed. Equation 1 was applied to determine $[Py]_{loc}$ for each Py-PA and $\langle k \rangle$ obtained from the MFA of the monomer and excimer fluorescence decays was plotted as a function of $[Py]_{loc}$ in THF, DMF, and DMSO. The $\langle k \rangle$ -vs- $[Py]_{loc}$ trends were linear in both DMF and DMSO, but deviations from linearity for the branched Py-PAs in THF led to the hypothesis of a difference in dynamics

between the secondary and tertiary amides. A molecular parameterization was applied to the Py-PAs to model the difference in dynamics between the tertiary and secondary amines by simulating a difference in the distance spanned by the tertiary amides w.r.t. the other Py-PA segments. Optimization of the tertiary amide span parameter b yielded the largest difference in amide dynamics in THF, which showed the strongest deviation from linearity. The trends in DMSO and DMF confirmed the validity of PEF as a means to assess the dynamics of pyrene-labeled molecules, in this instance specifically the Py-PAs. The good agreement between the $\langle k \rangle^{\text{exp-}v_S}$ - $[Py]_{\text{loc}}$ and $[Py]_{\text{loc}}^{\text{cal-}v_S}$ - $[Py]_{\text{loc}}$ trends implied that the molecular parameterization approach could quantify the difference in amide dynamics of the Py-PAs, opening the door for future studies of the internal dynamics of more complex PyLMs in solution.

REFERENCES

1. Winnik, M. A.; Redpath, T. The Dynamics of End-to-End Cyclization in Polystyrene Probed by Pyrene Excimer Formation. *Macromolecules* **1980**, *13*, 328-335.
2. Winnik, M. A.; Redpath, A. E. C.; Paton, K.; Danhelka, J. Cyclization dynamics of polymers: 10 Synthesis, fractionation, and fluorescent spectroscopy of pyrene end-capped polystyrenes. *Polymers* **1984**, *25*, 91-99.
3. Winnik, M. A. End-to-End Cyclization of Polymer Chains. *Acc. Chem. Res.* **1985**, *18*, 73-79.
4. Wilemski, G.; Fixman, M. Diffusion controlled intrachain reactions of polymers. I Theory. *J. Chem. Phys.* **1974**, *60*, 866-877.
5. Wilemski, G.; Fixman, M. Diffusion controlled intrachain reactions of polymers. II Results for a pair of terminal reactive groups. *J. Chem. Phys.* **1974**, *60*, 878-890.
6. Duhamel, J. New Insights in the Study of Pyrene Excimer Fluorescence to Characterize Macromolecules and their Supramolecular Assemblies in Solution. *Langmuir* **2012**, *28*, 6527-6538.
7. Thoma, J.; McNelles, S. A.; Adronov, A.; Duhamel, J. Direct Measure of the Local Concentration of Pyrenyl Groups in Pyrene-Labeled Dendrons Derived from the Rate of Fluorescence Collisional Quenching. *Polymers* **2020**, *12*, 2919.

Sanjay Patel
Chemistry
Waterloo

Conformation of PAMAM Dendrimers Probed
by Pyrene Excimer Formation

Conformation of PAMAM Dendrimers Probed by Pyrene Excimer Formation

Sanjay Patel and Jean Duhamel

Institute for Polymer Research, Waterloo Institute for Nanotechnology, Department of

Chemistry, University of Waterloo, ON N2L 3G1, Canada

INTRODUCTION

The conformation of macromolecules impacts their physical properties in solution and in the bulk. Hence, significant effort has been devoted to better understand their overall conformation in solution. To date the workhorse of macromolecular characterization in solution are scattering techniques, which provide invaluable information on macromolecular size and shape.¹ These scattering techniques probe the local density of a macromolecule with respect to its center of mass. Guinier's law can be applied to determine the radius of gyration (R_g), which is used as a benchmark to gauge how compact the macromolecule is. Although scattering experiments are applicable for most macromolecules, these techniques do have their limitations. Specifically, macromolecular objects must be sufficiently large to generate a strong scattering signal, be monodisperse, and often high concentrations ($\sim 1 - 20$ mg/mL) are required. An unfortunate aspect of working in this high concentration range, especially for polyelectrolytes, is that the macromolecules can aggregate, experience long range electrostatic interactions from neighbouring macromolecules, and be subject to other concentration related affects. These complications can significantly impede the characterization of macromolecules. Consequently, there is demand for experimental techniques that can provide complementary information about the conformation of a macromolecule in solution.

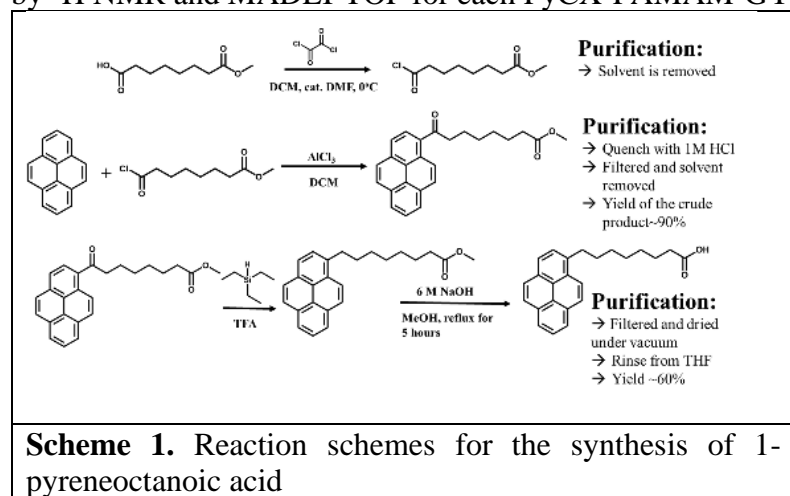
If the quantitative conformational information extracted from scattering techniques relies on the local density of a macromolecule, then, theoretically, any technique sensitive to the local density of a macromolecule should be able to provide insight about its conformation and conformational changes in solution. One such technique is fluorescence collisional quenching (FCQ). The use of FCQ to study macromolecules was promoted by the findings presented in 1974 by Wilemski and Fixman (WF), which suggested that the rate of encounter between a dye and its quencher covalently attached to the ends of a single, and thus monodisperse chain could be handled by a single rate constant,^{2,3} ushered a flurry of research activity focussed on the characterization of end labeled monodispersed samples.⁴ Although not explicitly stated in earlier work, the rate constant obtained for end labeled polymers depends also on the local quencher concentration, i.e., the local concentration of the chain end bearing the quencher experienced by the other chain end labeled with the dye. This would suggest that in FCQ studies of macromolecules labeled with multiple dyes and quenchers, each dye would sense the local concentration of the quenchers, which should in turn yield information about the overall conformation of the macromolecule in solution. Unfortunately, one inherent limitation suggested by the WF study is that macromolecules labeled with more than one dye-quencher pair would result in several rate constants whose values could not be extracted from the associated multiexponential decay. Although true, quantitative information about the conformation of macromolecules can still be obtained from the pseudo-unimolecular rate constant of pyrene excimer formation ($\langle k \rangle$), where pyrene excimer formation (PEF) is a classic example of FCQ. In this case, $\langle k \rangle$ is directly proportional to the local concentration of ground-state pyrenyl labels ($[Py]_{loc}$). In contrast to scattering techniques which work at high concentrations, studies with PEF work at significantly lower concentrations. For example, a concentration of ~ 10 - 20 g/L for polyamidoamine (PAMAM) dendrimers is typically used in SANS scattering experiments, whereas this concentration is reduced to 1.0×10^{-3} g/L for a fully pyrene-labeled PAMAM G0 dendrimer studied by PEF. This implies that the working concentration for PEF experiments can be 4 orders of magnitude lower than for SANS! At such a low concentration, PEF studies would be free of concentration-dependent effects, such as intermacromolecular aggregation and electrostatic repulsion between macromolecules.

In the present study, PEF was applied to characterize the conformation of a series of pyrene-labeled low generation PAMAM dendrimers referred to as PyCX-PAMAM-GY, where Y (= 0, 1, and 2) is the dendrimer generation number and X (= 4, 8, and 12) represents the number of carbon atoms in the linker connecting pyrene to the dendrimer. $\langle k \rangle$ was determined from the model free analysis (MFA) of the fluorescence decays acquired with the PyCX-PAMAM-GY samples and it was compared to $[Py]_{loc}$ taken as the ratio $n_{Py}/(\langle L_{Py}^2 \rangle^{1/2}/l)^3$, where n_{Py} is the number of ground-state pyrenes in a dendrimer, l is a normalization constant equivalent to a bond length, and $\langle L_{Py}^2 \rangle^{1/2}$ is the average end-to-end distance between every two pyrenyl labels. $\langle L_{Py}^2 \rangle$ was calculated by assuming that the internal segments constituting the dendrimer interior obeyed Gaussian statistics. The excellent correlation found between $\langle k \rangle$ and $n_{Py}/(\langle L_{Py}^2 \rangle^{1/2}/l)^3$ validated this assumption and provided a means to determine the radius of gyration and the end-to-end distance of these low generation PAMAM dendrimers. Consequently, this study represents the first quantitative characterization of the conformation of low generation PAMAM dendrimers by PEF, and perhaps more importantly, serves to demonstrate that PEF yields conformational insight about macromolecules in a manner that is complementary to scattering techniques, however at concentration that are orders of magnitude lower.

EXPERIMENTAL

Chemicals: PAMAM dendrimers of generation 0, 1, and 2 along with 1-pyrenebutyric acid were purchased from Sigma-Aldrich, while monomethyl suberate and 12-methoxy-12-oxodecanoic acid were purchased from Fisher Scientific and Ambeed chemicals, respectively.

Preparation of the pyrene-labeled PAMAM dendrimers: The synthesis of 1-pyreneoctanoic acid and 1-pyrenedodecanoic acid was adapted from a previous report⁵ and their synthesis is described in Scheme 1. The pyrene derivatives were attached onto the PAMAM dendrimers via an EDC-HCl coupling reaction and a brief description for the complete labeling of PAMAM-G0 with 1-pyrenebutyric acid is described hereafter. In brief, 20 mg of PAMAM-G0 (0.039 mmol, 4 eq of amine) was weighed into a 20 mL glass vial equipped with a magnetic stir bar. The dendrimer was dispersed in a mixture of DMSO (1 mL) and DMF (3 mL), followed by the addition of 1-pyrenebutyric acid (0.37 g, 0.93 mmol, 6 eq relative to the # of primary amines) and EDC-HCl (0.19 g, 1.0 mmol, 6.6 eq). The reaction was allowed to proceed at room temperature in the dark for 2 days followed by purification via 4-7 precipitations with diethyl ether (50 mL) followed by 3-4 rinses with deionized water (50 mL). The complete labeling of the dendrimer was confirmed by ¹H NMR and MADLI-TOF for each PyCX-PAMAM-GY sample.



Filter at 370 and 495 nm, respectively, to minimize stray light from reaching the detector. The decays were globally analyzed using the model free analysis (MFA), which has been described

Fluorescence experiments:

Solutions of 2.5×10^{-6} M of the PyCX-PAMAM-GY samples were prepared in DMF or DMSO, which were degassed under nitrogen for 30-45 min before conducting fluorescence measurements. The fluorescence decays of the pyrene monomer and excimer were acquired by exciting the solutions at 336 nm and monitoring the emission at 379 nm and 510 nm with a cut-off

elsewhere in more detail.⁶ $\langle k \rangle$ was calculated for each PyCX-PAMAM-GY sample according to the MFA of the fluorescence decays and compared with $[Py]_{loc}$.

RESULTS AND DISCUSSION

The PyCX-PAMAM-GY constructs were parameterized in the same manner as done earlier to determine $[Py]_{loc}$. **Error! Bookmark not defined. Error! Bookmark not defined.** In brief, $[Py]_{loc}$ was calculated with Equation 1, where $[Py]_{loc}$ is equal to the number n_{Py} of ground-state pyrenes over the dendrimer volume. The dendrimer was assumed to occupy a spherical volume with a diameter equal to its average end-to-end distance ($\langle L_{Py}(N)^2 \rangle^{1/2}$). $\langle L_{Py}(N)^2 \rangle$ was calculated by taking the internal segments constituting the dendrimer interior as linear chains obeying Gaussian statistics and its expression is given in Equation 2. In Equation 2, b ($= 7$) and c ($= 4$) correspond to the number of atoms in the aminoethyl propionamide building block and ethylene diamine core in the PAMAM dendrimer, respectively, whereas a corresponds to the number of carbon atoms in the linker of the pyrene derivative set to equal 4, 8, or 12 for the 1-pyrene-butyryl, -octanoyl, or -dodecanoyl derivatives, respectively. N represents the generation number of the dendrimer. The ratio $n_{Py}/(\langle L_{Py}^2 \rangle^{1/2}/l)^3$ was taken as a measure of $[Py]_{loc}$, where l is a normalization factor corresponding to a bond length.

$$[Py]_{loc} = \frac{n_{Py}}{V_{dendrimer}} = \frac{2^{N+2} - 1}{4\pi \left(\frac{\langle L_{Py}^2(N) \rangle^{1/2}}{2} \right)^3} \sim \frac{n_{Py}}{(\langle L_{Py}^2 \rangle^{1/2} / l)^3} \quad (1)$$

$$\langle L_{Py}^2(N) \rangle = \left(2a + \frac{[2 - 2^{N+2} + (N+1) \times 2^{N+3}]b + 2^{N+1}c + 2^{N+1} - 1}{2^{N+2} - 1} \right) \times l^2 \quad (2)$$

To validate the assumption that the PAMAM dendrimer segments obey Gaussian statistics, $R_g(N)$, the radius of gyration of a PAMAM dendrimer of generation N was calculated with Equation 3, and compared with $R_g(N)$ obtained by molecular dynamic simulations (MDS). **Error! Bookmark not defined.** It should be noted that the $R_g(N)$ determined by MDS had been compared with the experimental $R_g(N)$ obtained by SAXS for high generation dendrimers. **Error! Bookmark not defined. Error! Bookmark not defined.** As seen in Figure 1, $R_g(N)/l$ obtained with Equation 3 showed excellent agreement with the $R_g(N)$ values obtained from MDS up to the PAMAM-G4 dendrimer. The deviation observed after the PAMAM-G4 dendrimer must be due to interior crowding of the higher generation dendrimers, which prevents the chains from adopting a Gaussian conformation, an explicit assumption for Equation 3. The excellent agreement between the $R_g(N)/l$ values obtained with Equation 3 and $R_g(N)$ obtained from MDS for the lower generation dendrimers supports the assumption made to derive Equation 1, that the internal segments of low generation PAMAM dendrimers obey Gaussian statistics.

$$R_g(N) = \frac{2 \times \left[2^{N+1} \sum_{i=1}^{c/2+(N+1) \times b} \sqrt{i} - \sum_{k=0}^N 2^k \sum_{i=1}^{c/2+k \times b} \sqrt{i} \right]}{c + 4(2^{N+1} - 1)} \times l \quad (3)$$

$\langle k \rangle$ obtained in DMF and DMSO for the PyCX-PAMAM-GY samples was plotted as a function of $n_{Py}/(\langle L_{Py}(N)^2 \rangle^{1/2}/l)^3$ in Figures 2A and B, respectively. Good correlations between $\langle k \rangle$ and $n_{Py}/(\langle L_{Py}(N)^2 \rangle^{1/2}/l)^3$ were obtained. These trends were compared with those previously obtained with pyrene-labeled dendrimers prepared with a *bis*-(hydroxymethyl)propionic acid backbone and labeled with 1-pyrenebutyric acid (PyC4-HMPA-GY).^{7,8} All $\langle k \rangle$ values obtained with the PyC4-HMPA-GY dendrimers clustered around the same straight line as that obtained with

the PyCX-PAMAM-GY samples when plotted against $n_{\text{Py}}/(\langle L_{\text{Py}}(N)^2 \rangle^{1/2}/l)^3$. This result further validated the approach used to parameterize the PyCX-PAMAM-GY and PyC4-HMPA-GY dendrimers to obtain $\langle L_{\text{Py}}^2 \rangle$.

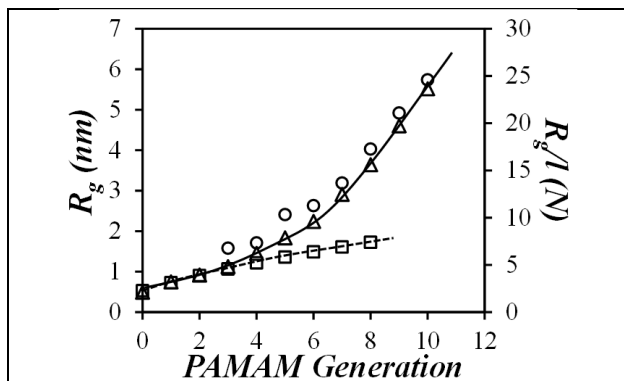


Figure 1. Comparison of R_g determined via (○) SAXS,⁹ (△) computer simulations,¹⁰ and (□) with Equation 6.

However, the solvent-induced differences between the viscosity and the probability of PEF upon pyrene-pyrene encounter meant that the trends obtained in DMF in Figure 2A and DMSO in Figure 2B had different slopes. The differences in the slopes could be accounted for by dividing $\langle k \rangle$ by k_{diff} , the PEF bimolecular rate constant for a model compound. k_{diff} for hexyl 1-pyrenebutyramide used as model compound was found to equal $1.05 (\pm 0.01)$ and $0.700 (\pm 0.003) \text{ M}^{-1} \cdot \text{ns}^{-1}$ in DMF and DMSO, respectively. Plotting $\langle k \rangle/k_{\text{diff}}$, which no longer depended on solvent viscosity and PEF probability, as a function of $n_{\text{Py}}/(\langle L_{\text{Py}}(N)^2 \rangle^{1/2}/l)^3$ yielded a master line,

as seen in Figure 2C, where the $\langle k \rangle/k_{\text{diff}}$ ratios of all PyCX-PAMAM-GY and PyC4-HMPA-GY samples clustered along a single master line. A Pearson correlation coefficient of 0.99 between $\langle k \rangle/k_{\text{diff}}$ and $n_{\text{Py}}/(\langle L_{\text{Py}}(N)^2 \rangle^{1/2}/l)^3$ was found. The near unity Pearson correlation coefficient demonstrates that $\langle k \rangle/k_{\text{diff}}$ is directly related to $[Py]_{\text{loc}}$. Furthermore, since these macromolecules were covalently labeled with pyrene, $[Py]_{\text{loc}}$ also yields conformational information about the PAMAM and HMPA dendrimers. For example, $\langle k \rangle/k_{\text{diff}}$ for PyC4-PAMAM-G1 and PyC4-HMPA-G3, both sharing a same number of 8 pyrenyl labels, equals 0.18 and 0.38, respectively. Since $\langle k \rangle$ is proportional to $[Py]_{\text{loc}}$, the higher $\langle k \rangle/k_{\text{diff}}$ ratio obtained for PyC4-HMPA-GY suggests that the PyC4-HMPA-GY dendrimers adopt a more compact conformation, resulting in a higher $[Py]_{\text{loc}}$, compared to the PyC4-PAMAM-GY dendrimers.

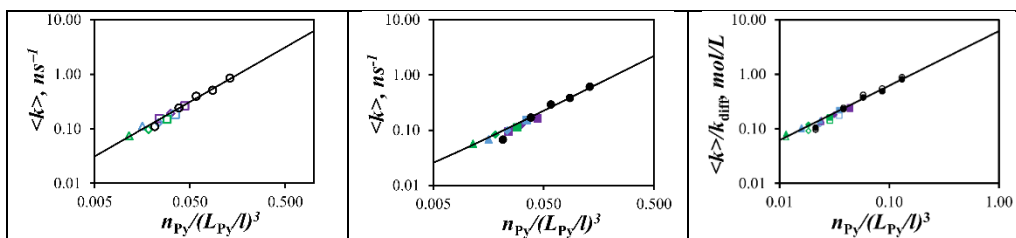


Figure 2. Plot of $\langle k \rangle$ as a function of $n_{\text{Py}}/(\langle L_{\text{Py}}(N)^2 \rangle^{1/2}/l)^3$ for the PyCX-PAMAM-GY and PyC4-HMPA-GY samples in A) DMF and B) DMSO. C) Plot of $\langle k \rangle/k_{\text{diff}}$ as a function of $n_{\text{Py}}/(\langle L_{\text{Py}}(N)^2 \rangle^{1/2}/l)^3$ for the PyCX-PAMAM-GY and PyC4-HMPA-GY samples in (hollow symbols) DMF and (filled symbols) DMSO. △, ◇, and □ represent PAMAM-GY with $Y = 0, 1,$ and $2,$ respectively, while purple, blue, and green represent PyCX-PAMAM-GY dendrimers labeled with 1-pyrene-butyric, -octanoic, and -dodecanoic acid, respectively. Data for PyC4-HMPA-GY samples in (○) DMF and (●) DMSO.^{7,8}

The trends shown in Figure 2C clearly illustrate that $\langle k \rangle/k_{\text{diff}}$ obtained for the PyCX-PAMAM-GY and PyC4-HMPA-GY dendrimers respond to $[Py]_{\text{loc}}$ and since $[Py]_{\text{loc}}$ was obtained through the derivation of $\langle L_{\text{Py}}^2 \rangle$, $[Py]_{\text{loc}}$ reflects not only conformational differences between different macromolecules but also within a same macromolecule experiencing different solution conditions. The validity of this statement was assessed by monitoring changes in $\langle k \rangle$ in Figures

3A and B for the PyCX-PAMAM-GY dendrimers in, respectively, DMF and DMSO with or without 5 mM HCl. These experiments were conducted to provide additional experimental support to numerous reports, which have indicated that protonation of either the interior tertiary or exterior primary amines of the PAMAM dendrimers induces a conformational change in the dendrimers.¹¹⁻¹⁴ Visual inspection of Figures 3A and B demonstrated that with 5 mM HCl, $\langle k \rangle$ increases linearly with $n_{\text{Py}}/(\langle L_{\text{Py}}(N)^2 \rangle^{1/2}/l)^3$, however with a notably lower slope than without HCl. Solvent differences were accounted for by considering the $\langle k \rangle/k_{\text{diff}}$ ratio, where k_{diff} was obtained for hexyl 1-pyrenebutyramide in DMF and DMSO with and without 5 mM HCl. The values of $1.05 (\pm 0.01)$ and $0.700 (\pm 0.003) \text{ ns}^{-1} \cdot \text{M}^{-1}$ obtained for k_{diff} in DMF and DMSO without HCl were equal, within experimental error, to those of $1.06 (\pm 0.01)$ and $0.71 (\pm 0.01) \text{ ns}^{-1} \cdot \text{M}^{-1}$ in DMF and DMSO with 5 mM HCl, respectively. Plotting $\langle k \rangle/k_{\text{diff}}$ as a function of $n_{\text{Py}}/(\langle L_{\text{Py}}(N)^2 \rangle^{1/2}/l)^3$ in Figure 3C indicated that the $\langle k \rangle/k_{\text{diff}}$ ratios obtained in DMF and DMSO with 5 mM HCl were clustered around a single master line, whose slope was smaller than the master line obtained without HCl. Since $\langle k \rangle/k_{\text{diff}}$ is independent of solvent effects, the $\langle k \rangle/k_{\text{diff}}$ ratios under each condition were averaged and the averaged values were plotted as a function of $n_{\text{Py}}/(\langle L_{\text{Py}}(N)^2 \rangle^{1/2}/l)^3$ in Figure 3D. Pearson correlation coefficients of 0.99 and 0.98 were obtained for the trends without and with 5 mM HCl, respectively, suggesting that the assumption, that the internal segments of the PAMAM dendrimers obeyed Gaussian statistics, was still valid for the dendrimers in DMF and DMSO with 5 mmol HCl. The 67% decrease in the slope observed upon protonation of the tertiary amines within the interior of the dendrimer reflected a decrease in $[\text{Py}]_{\text{loc}}$ resulting from intra-electrostatic repulsion inducing a swelling of the dendrimer volume. A 67% increase in the dendrimer volume suggested a 14% increase in its length scale being either R_g or $\langle L_{\text{Py}} \rangle^{1/2}$ upon protonation of the tertiary amines. This increase in the dendrimers radius upon protonation of the internal tertiary amines determined via PEF is in excellent agreement with MDS of the PAMAM-GY dendrimers with $Y = 4, 5,$ and 6 for which R_g had been found to increase by, respectively, 13%, 20% and 15% between unprotonated and fully protonated dendrimers.¹⁴ This good agreement further supports the notion that PEF can provide quantitative conformational information about macromolecules in solution in a manner that is complementary to scattering techniques, however with the distinct advantage of working with significantly lower concentrations.

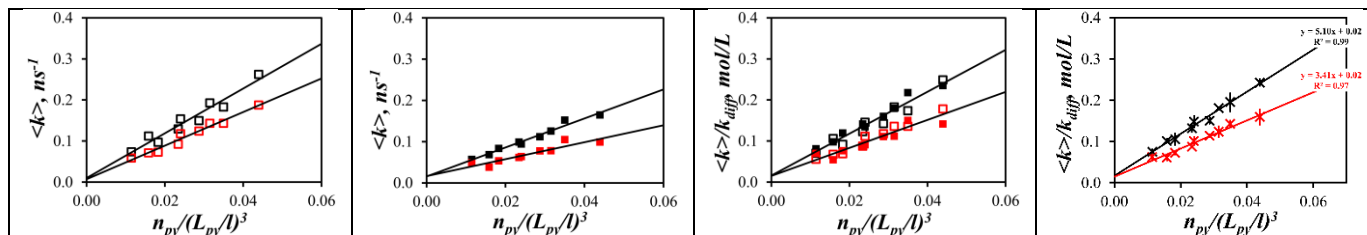


Figure 3. Plot of $\langle k \rangle$ as a function of $n_{\text{Py}}/(\langle L_{\text{Py}}(N)^2 \rangle^{1/2}/l)^3$ for the PyCX-PAMAM-GY samples in A) (empty squares) DMF and B) (filled squares) DMSO (black) without and (red) with 5 mM HCl. C) Plot of $\langle k \rangle/k_{\text{diff}}$ as a function of $n_{\text{Py}}/(\langle L_{\text{Py}}(N)^2 \rangle^{1/2}/l)^3$ for the PyCX-PAMAM-GY samples in DMF and DMSO. D) Plot of the $\langle k \rangle/k_{\text{diff}}$ ratio averaged with the values in DMF and DMSO (\blackstar) without and (\redstar) with 5 mM HCl.

CONCLUSIONS

PEF was used to study a series of PyCX-PAMAM-GY dendrimers, where $Y (= 0, 1,$ and $2)$ and $X (= 4, 8,$ and $12)$ represent the dendrimer generation and the number of carbon atoms in the pyrene derivative linker, respectively. These studies demonstrated that the pseudo-unimolecular rate concentration of excimer formation, $\langle k \rangle$, is directly proportional to $[\text{Py}]_{\text{loc}}$. Since $[\text{Py}]_{\text{loc}}$ reflects the local density of a macromolecule, $\langle k \rangle$ can be used to gain conformational information about complex macromolecules like low generation PAMAM dendrimers in a manner that is complementary to SAXS and SANS.

REFERENCES

1. Boldon, L.; Labliberte, F.; Lie, Li. Review of the Fundamental Theories behind small angle X-ray scattering, molecular dynamics simulations, and relevant integrated application. *Nano. Rev.* **2014**, *6*, 1-38.
2. Wilemski, G.; Fixman, M. Diffusion-Controlled Intrachain Reactions of Polymers. I Theory. *J. Chem. Phys.* **1974**, *60*, 866–877.
3. Wilemski, G.; Fixman, M. Diffusion-Controlled Intrachain Reactions of Polymers. II Results for a Pair of Terminal Reactive Groups. *J. Chem. Phys.* **1974**, *60*, 878–890.
4. Winnik, M. A. End-to-End Cyclization of Polymer Chains. *Acc. Chem. Res.* **1985**, *18*, 73-79.
5. Lau, G. C.; Sather, N. A.; Sai, H.; Waring, E. M.; Deiss-Yehiely, E.; Barreda, L.; Beeman, E. A.; Palmer, L. C.; Stupp, S. I. Oriented Multiwalled Organic–Co(OH)₂ Nanotubes for Energy Storage. *Adv. Funct. Mater.* **2018**, *28*.
6. Duhamel, J. Internal Dynamics of Dendritic Molecules Probed by Pyrene Excimer Formation. *Polymers* **2012**, *4*, 211-239.
7. Thoma, J.; McNelles, S. A.; Adronov, A.; Duhamel, J. Direct Measure of the Local Concentration of Pyrenyl Groups in Pyrene-Labeled Dendrons Derived from the Rate of Fluorescence Collisional Quenching. *Polymers* **2020**, *12*, 2919.
8. McNelles, S. A.; Thoma, J. L.; Adronov, A.; Duhamel, J. Quantitative Characterization of the Molecular Dimensions of Flexible Dendritic Macromolecules in Solution by Pyrene Excimer Fluorescence. *Macromolecules* **2018**, *51*, 1586–1590.
9. Prosa, T. J.; Bauer, B. J.; Amis, E. J.; Tomalia, D. A.; Scherrenberg, R. A SAXS Study of the Internal Structure of Dendritic Polymer Systems. *J. Polym. Sci. B, Part B: Polym. Phys.* **1997**, *35*, 2913-2924
10. Maiti, P. K.; Çağın, T.; Wang, G.; Goddard, W. A. Structure of PAMAM Dendrimers: Generations 1 through 11. *Macromolecules* **2004**, *37*, 6236–6254.
11. Liu, Y.; Bryantsev, V. S.; Diallo, M. S.; Goddard, W. A. PAMAM Dendrimers Undergo PH Responsive Conformational Changes Without Swelling. *J. Am. Chem. Soc.* **2009**, *131*, 2798–2799.
12. Porcar, L.; Hong, K.; Butler, P. D.; Herwig, K. W.; Smith, G. S.; Liu, Y.; Chen, W. R. Intramolecular Structural Change of PAMAM Dendrimers in Aqueous Solutions Revealed by Small-Angle Neutron Scattering. *J. Phys. Chem. B* **2010**, *114*, 1751–1756.
13. Welch, P.; Muthukumar, M. Tuning the Density Profile of Dendritic Polyelectrolytes. *Macromolecules* **1998**, *31*, 5892-5897.
14. Maiti, P.; Çağın, T.; Lin, S-T.; Goddard, W. Effect of Solvent and pH on the Structure of PAMAM Dendrimers. *Macromolecules* **2005**, *38*, 979-991.

Donghan Liu
Chemistry
Waterloo

Conformation of Poly(γ -Benzyl Glutamate) in Organic Solvents

Conformation of Poly(γ -benzyl glutamate) in Organic Solvents

Donghan Liu and Jean Duhamel

Institute for Polymer Research, Waterloo Institute for Nanotechnology, Department of Chemistry, University of Waterloo, 200 University Avenue West, Waterloo, ON N2L 3G1

INTRODUCTION

Dilute solutions of macromolecules offer an experimental means to characterize their conformation as isolated molecules, allowing a better understanding of their behaviour and properties in solution but also in the bulk phase. This structure-property relationship has been established for numerous macromolecules including proteins such as gelatin.¹ Gelatin forms triple-helices that generate a hydrogel in water, but their disruption with $\text{Fe}(\text{NO}_3)_3$ can lead to the formation of a viscoelastic liquid, a transition that has found application in material chemistry.² In another example, trifluoroacetic acid was added to a solution of the block copolymer poly(γ -benzyl-*L*-glutamate)-*b*-poly(ethylene glycol) to induce the polypeptide block to undergo a conformational change from a rigid helix to a random coil. In turn, this conformational transition led to a significant change in the shape of the block copolymer micelles formed in ethanol as shown in Figure 1.³ These examples illustrate why extensive research has been carried out over the years to develop reliable methods to probe the conformation of macromolecules in solution.

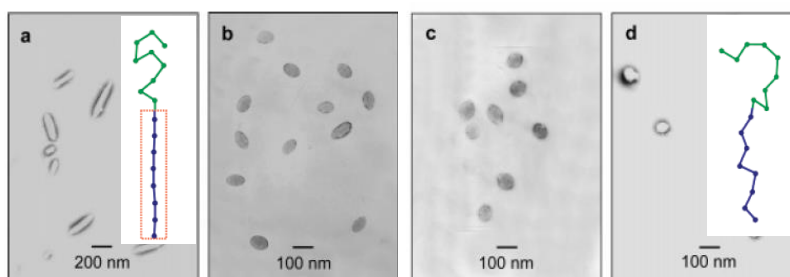


Figure 1. TEM pictures showing ellipsoidal micelles formed by poly(γ -benzyl-*L*-glutamate)-*b*-poly(ethylene glycol) in ethanol with a) no TFA, b) 0.017 mole fraction of TFA, c) 0.033 mole fraction of TFA, and spherical micelles formed by poly(γ -benzyl-*L*-glutamate)-block-poly(ethylene glycol) in ethanol with a 0.066 mole fraction of TFA.

Among the conventional techniques applied to probe the conformation of macromolecules in solution are scattering methods (static (SLS) and dynamic (DLS) light scattering and small angle X-ray (SAXS) and neutron (SANS) scattering), circular dichroism (CD), intrinsic viscosity, or NMR. All these techniques have their advantages and disadvantages, but one common feature is the 1 – 10 g/L range of polymer concentrations needed to generate sufficient signal for analysis. In contrast, fluorescence can probe macromolecules at concentrations within 1 – 10 mg/L, 3-to-4 orders of magnitude lower. The question however remains as to whether fluorescence techniques can provide quantitative conformational information about macromolecules in solution. This work focuses on pyrene excimer formation (PEF) and its potential to provide quantitative structural information on macromolecules in solution. While the main disadvantage of PEF is the additional step of having to label the macromolecule with a pyrene derivative, its advantages include a high sensitivity enabling the study of 1 – 5 mg/L polymer solutions and the possibility of studying monodisperse but also polydisperse macromolecules. In this example, PEF is applied to characterize the conformation of poly(γ -benzyl *L*-glutamate) (PLBG) and poly(γ -benzyl *D,L*-glutamate) (PBDLG) randomly labeled with pyrene in various organic solvents. PBLG and PBDLG are expected to adopt an α -helical and a random coil conformation, respectively. Thanks

to the benzyl side chain, PBLG and PBDLG should be soluble in a wider range of organic solvents compared to poly(glutamic acid), which dissolves mainly in *N,N*-dimethyl formamide (DMF) or dimethyl sulfoxide (DMSO). Establishing that PEF can characterize the conformation of PBLG and PBDLG in a variety of organic solvents will enable the extension of this study to the conformational characterization of PBLG and PBDLG in the hydrophobic microenvironment generated by surfactant micelles or lipid vesicles in aqueous solution in an effort to approach conditions mimicking the environment experienced by membrane proteins in a cell.

EXPERIMENTAL

Chemicals: Butylamine (99.5%), 1-pyrenemethanol (98%), 1-pyrenebutanol (99%), α -pinene (98%), trifluoroacetic acid (TFA, 99%), diisopropylcarbodiimide (DIC, 99%), dimethyl sulfoxide (DMSO, 99%), *N,N*-dimethyl formamide (DMF, 99.9%), 1,4-dioxane (99%), diethyl ether (with butylated hydroxytoluene (BHT) as inhibitor, 99%), hexanes (mixture of isomers, 98.5%), tetrahydrofuran (THF, 99%), dichloromethane (DCM, 99.8%), ethyl acetate (99.7%), acetone (99.9%), toluene (99.5%), *d*₆-DMSO (99.9 atom% deuterium), and chloroform-*d* (99.9 atom% deuterium) were purchased from Sigma-Aldrich. *L*-Glutamic acid- γ -benzyl glutamate (H-Glu(OBzl)-OH, 97%) and triphosgene (99%) were acquired from Oakwood chemical. Acetic anhydride (97%) and tetrahydrofuran for spectroscopy measurements (fluorescence grade, inhibitor-free) were purchased from Fisher Scientific. *D*-glutamic acid- γ -benzyl glutamate (H-Glu(OBzl)-OH, 98%) was purchased from BLDpharm.

Synthesis of the pyrene-labeled polypeptides: Pure γ -benzyl-*L*-glutamate or an equimolar mixture of γ -benzyl-*L*-glutamate and γ -benzyl-*D*-glutamate were converted into their corresponding *N*-carboxy anhydride (NCA) by dissolving them in ethyl acetate and refluxing the mixture with triphosgene and α -pinene for 3 hours. The reaction mixtures were then filtered with a 0.22 μ m PTFE filter before being precipitated 6 times in hexane. The purified NCAs were dried in a vacuum oven for 16 hours before being dissolved in distilled DMF in a round bottom flask under dry nitrogen. PBLG and PBDLG were synthesized by polymerizing the corresponding NCA in DMF using *N*-hexylamine as initiator. When the polymerization was complete, the amine end of the polypeptide chain was capped by reacting it with a 30 molar excess of acetic anhydride for 12 hours. Each polypeptide was precipitated in ether 4 times before being partially deprotected with trifluoroacetic acid to generate a series of polypeptide samples with various degrees of deprotection before conducting four additional precipitations in ether. The resulting polypeptides with free acid groups were labeled with 1-pyrenemethanol or 1-pyrenebutanol using diisopropylcarbodiimide (DIC) as coupling agent in a 95:5 DCM:DMF mixture with 0.1 molar equivalent of DMAP per acid group as described in Figure 3. The pyrene labeled polypeptides with different pyrene contents were purified by 4 ether and 4 ethanol precipitations.

Polypeptide characterization: The chemical composition of the polypeptides was characterized by ¹H NMR and their molecular weight distribution was determined with a gel permeation chromatography (GPC) instrument equipped with a light scattering, refractive index, and viscosity detector. The pyrene content of the polypeptide samples was determined by UV-Vis spectroscopy.

Fluorescence measurements: The pyrene-labeled poly(benzyl glutamate) (Py-PBG) samples were excited at 344 nm. First, their steady-state fluorescence spectra were acquired by scanning the fluorescence intensity from 350 to 650 nm. The fluorescence decays of the pyrene monomer and excimer of the Py-PBG samples were acquired with an emission wavelength set at 375 and 510 nm and with a cutoff filter at 370 and 495 nm, respectively. The fluorescence decays of the pyrene monomer and excimer were analyzed globally according to the Fluorescence Blob Model (FBM) to determine the maximum number (N_{blob}) of structural units separating two pyrenyl labels while still allowing PEF. N_{blob} reflects the conformation of the Py-PBG samples.

Molecular mechanics optimizations: Molecular mechanics optimizations (MMO) were conducted with HyperChem to predict the theoretical $N_{\text{blob}}^{\text{theo}}$, that would be obtained for an α -helical and a randomly coiled PBG. To this end, two constructs with 36 benzyl glutamates were prepared that would adopt an α -helical and a random coil conformation. One benzyl side chain toward one end of the construct was replaced with a 1-pyrenemethyl or 1-pyrenebutyl group, which was considered as the reference pyrene. The benzyl group of the next benzyl glutamate was replaced

by a second pyrenyl group and the two pyrenes were induced to come within 3.4 Å from each other. The number of carbons from the reference pyrene overlapping the frame of the second pyrene was determined. The process was repeated by moving the second pyrenyl derivative to the next benzyl glutamate one unit at a time, until no overlap could be found between the reference pyrene and the secondary pyrene. The number of positions enabling a number of overlapping carbon atoms larger than 7 was counted to give N_o . $N_{\text{blob}}^{\text{theo}}$ was taken as $2 \times N_o + 1$ where N_o was double to account for the symmetry of the polypeptide backbone with respect to the position of the reference pyrene and 1 was added to represent the structural unit bearing the reference pyrene.

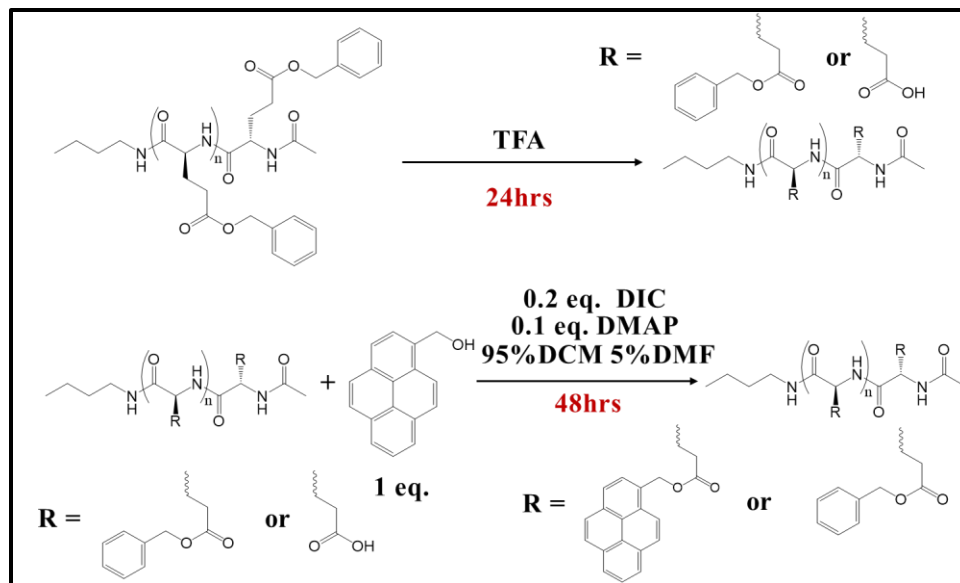


Figure 3. Deprotection and pyrene labeling of PBLG.

RESULTS AND DISCUSSION

Successful synthesis of PBG samples was demonstrated by analysis of the ^1H NMR spectra. The ^1H NMR spectrum of PBDLG in d_6 -DMSO is shown as an example in Figure 3 where all peaks were assigned. Integration of the signal corresponding to the hydrogens of the benzyl-*DL*-glutamate structural units matched the expected composition based on the chemical structure and no significant impurity was observed. Analysis of the gel permeation chromatography traces obtained with a light scattering, differential refractive index, and viscosity detector of the PBDLG and PBLG samples in DMSO yielded a degree of polymerization of 150 (± 15) and a polydispersity index (PDI) of 1.05.

A small portion of each PBG was then labeled with 1-pyrenemethanol or 1-pyrenebutanol as described in the Experimental section. The pyrene labeled PBGs were characterized by GPC and the absence of an absorption peak in the low molecular weight region of the GPC traces acquired with a UV-Vis detector indicated that the pyrene labeled polypeptides were free of unreacted pyrene derivative. The pyrene content of the PBLG sample labeled with 1-pyrenebutanol was found to equal 14.0 and 16.8 mol%, respectively. The pyrene content of the PBDLG labeled with 1-pyrenemethanol had a pyrene content of 14.6 mol%. The PBLG sample labeled with 1-pyrenemethanol were then dissolved in various organic solvents and characterized by SSF. The fluorescence spectra are shown in Figure 4A and they were normalized at 377 nm corresponding to the 0-0 transition of pyrene.

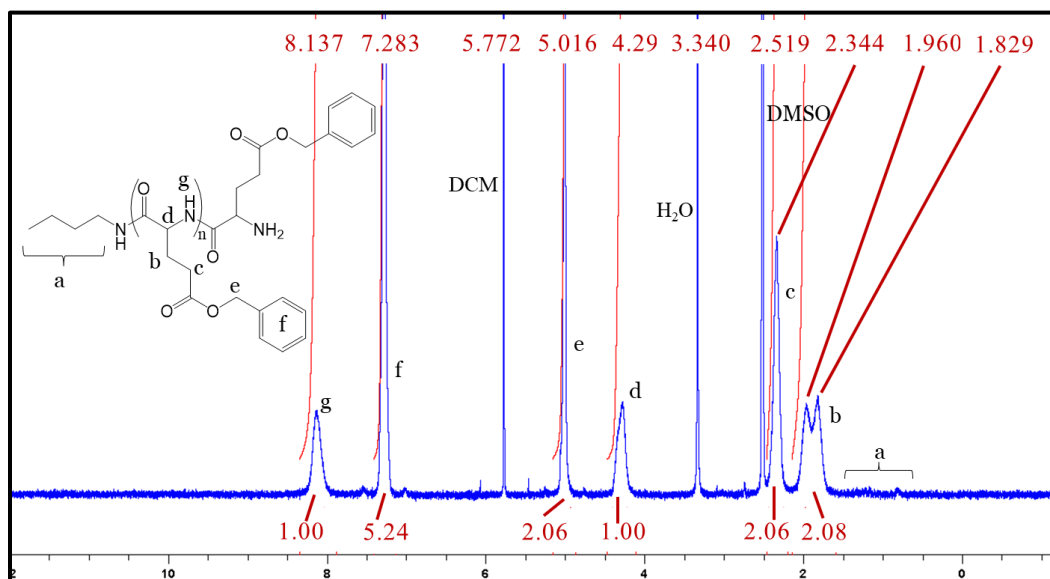


Figure 3. ¹H NMR spectrum of PBDLG in *d*₆-DMSO.

The fluorescence spectra show the typical sharp fluorescence peaks between 370 and 410 nm characteristic of the pyrene monomer and the broad structureless emission of the pyrene excimer centered at 480 nm. The excimer emission was found to increase with decreasing solvent viscosity relative to the monomer emission. This effect could be more clearly visualized in Figure 4B, where the fluorescence intensity ratio (I_E/I_M) of the pyrene excimer over the pyrene monomer was plotted as a function of the inverse of the solvent viscosity (η). To calculate the I_E/I_M ratio, the fluorescence intensity (I_E) of the excimer was integrated from 500 to 530 nm and the fluorescence intensity of the first monomer peak in Figure 4A was integrated from 374 to 380 nm. A trend was obtained where the I_E/I_M ratio increased linearly with increasing η^{-1} for the organic solvents.⁴ This result was expected since pyrene excimer formation is a diffusion-controlled process and the I_E/I_M ratio is proportional to the product $k_{\text{diff}} \times [\text{Py}]_{\text{loc}}$, where k_{diff} is the bimolecular rate constant for pyrene excimer formation and $[\text{Py}]_{\text{loc}}$ is the local concentration of ground-state pyrene experienced by an excited pyrene bound to the polypeptide. The trends shown in Figure 4B demonstrates that the fluorescence signal of the pyrene-labeled polypeptides responds to their local environment, in this case the solvent viscosity.

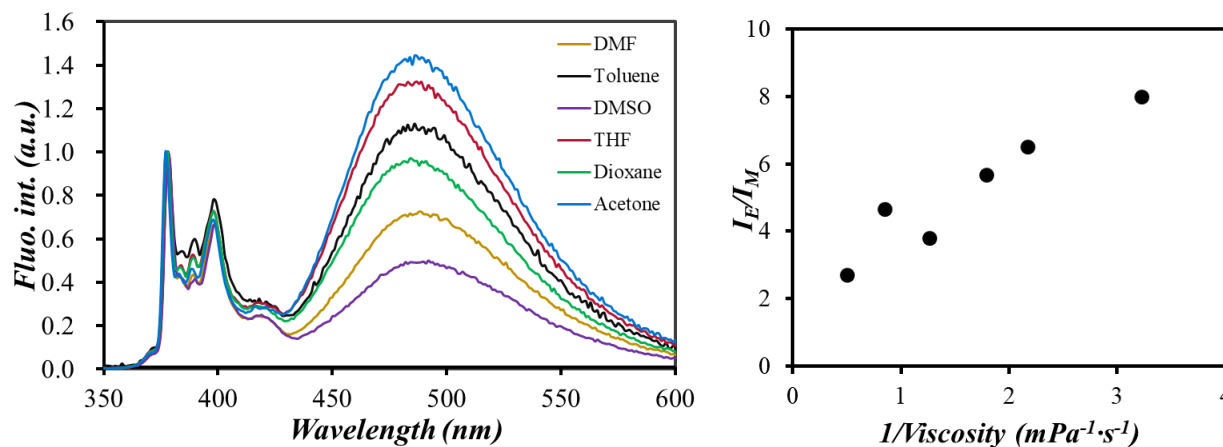


Figure 4. A) Fluorescence spectra of the PBLG sample labeled with 1-pyrenemethanol in different organic solvents and B) plot of the I_E/I_M ratio as a function of the inverse of the solvent viscosity.

The fluorescence decays of the pyrene-labeled polypeptides were acquired and analyzed according to the fluorescence blob model (FBM) to determine N_{blob} , the number of structural units in the volume probed by an excited pyrene. N_{blob} is taken as a measure of the local density of the macromolecular construct and is thus a measure of its conformation. An N_{blob} value of 17 was found for Py-PBLG with a pyrene content of 16.8% in DMF, where the peptide should adopt an α -helical conformation. In contrast, a theoretical value of 27 was predicted for an α -helical conformation by MMO. For Py-PBDLG in DMF, the experimental and theoretical N_{blob} value were 19 and 15, respectively.

The fact that the experimental N_{blob} values equal $18 (\pm 1)$ for both the α -helical Py-PBLG and the randomly coil Py-PBDLG samples suggests that the pyrenyl labels do not respond to the change in density occurring as the polypeptide changes its conformation, as had been observed for pyrene-labeled samples of poly(*L*-glutamic acid) and poly(*D,L*-glutamic acid). It might be that the bulky benzyl side chains appear to limit the mobility of the pyrenyl labels preventing its ability to sense the local conformation of the polypeptide it is attached to.

Another potential reason as to why the PBG samples might appear to be unresponsive to the conformation of the polypeptides might be due to the non-random deprotection of the benzyl esters by TFA before pyrene-labeling. If deprotection occurred in a more clustered manner, it would distort the expected random distribution of the pyrenyl labels and would result in a lack of sensitivity of the pyrene response to the macromolecular conformation, as was observed with the Py-PBG samples. To address this possibility, a synthesis route will be attempted whereby all benzyl group of the PBG samples will be removed to yield the naked poly(glutamic acid) backbone that will be labeled with 1-pyrenemethylamine before reacting the remaining glutamic acids with benzyl alcohol to create a Py-PBG sample where the pyrenyl labels are randomly attached.

CONCLUSION

These preliminary results indicate that two PBG samples were successfully synthesized and labeled with pyrene derivatives. Fluorescence experiments conducted with the PBLG samples labeled with 1-pyrenemethanol showed that the I_E/I_M ratio is inversely proportional to solvent viscosity, indicating that the pyrene-labeled construct responded to its local environment. However, time-resolved fluorescence measurements indicated that the pyrene-labeled PBG samples did not respond to changes in conformation of the polypeptides. To assess whether this lack of response to conformational changes was due to the non-random labeling of the PBG samples, a synthetic strategy was proposed to generate PBG samples, where the pyrenyl labels would be randomly attached.

REFERENCES

1. Borgia, M., Borgia, A., Best, R. *et al.* Single-molecule fluorescence reveals sequence-specific misfolding in multidomain proteins. *Nature*, 2011, 474, pp. 662–665.
2. Danks, A. E., Hollamby, M. J., Hammouda, B., Fletcher, D. C., Johnston-Banks, F., Rogers, S. E., Schnepf, Z. Mechanistic insights into the formation of porous carbons from gelatin. *J. Mater. Chem*, 2011, 5(23), pp. 11644–11651.
3. W. Ding, S. Lin, J. Lin, L. Zhang. Effect of Chain Conformational Change on Micelle Structures: Experimental Studies and Molecular Dynamics Simulations. *J. Phys. Chem*, 2008, 112(3), pp. 776-783.
4. CRC Handbook of Chemistry and Physics 58th ed.; Weast, R. C., Ed. CRC Press: Boca Raton, FL, 1978; p E39-41.

